Title
Transfer Kinetics and Analysis of Solid-Solid Electrochemical Interfaces

Author
Ware, Nicholas Abraham

Publication Date
2021

Peer reviewed|Thesis/dissertation

UNIVERSITY OF CALIFORNIA

Los Angeles

Transfer Kinetics and Analysis of Solid-Solid Electrochemical Interfaces

A thesis submitted in partial satisfaction

of the requirements for the degree Master of Science

in Materials Science and Engineering

by

Nicholas Abraham Ware

2021

ABSTRACT OF THE THESIS

Transfer Kinetics and Analysis of Solid-Solid

Electrochemical Interfaces

by

Nicholas Abraham Ware

Master of Science in Materials Science and Engineering

University of California, Los Angeles, 2021

Dr. Bruce S. Dunn, Chair

A nontraditional double potential step (DPS) methodology along with two more commonly used approaches for examining interface kinetics in battery materials are presented and applied to the well-studied systems of lithium cobalt oxide, Li_xCoO_2, and LiPON solid electrolyte. Values for the heterogeneous rate constants of Li_xCoO_2 at the nonaqueous $PC/LiClO_4$ and solid electrolyte interfaces are determined and equivalencies between electrochemical impedance spectroscopy (EIS), the method of Nicholson, and the double potential step measurements of interfacial kinetics are elucidated, while a qualitative mechanistic understanding of the heterogeneous rate constant is discussed. The anodic and cathodic heterogeneous rate constants for the $PC/LiClO_4$ – Li_xCoO_2 interface were $1.1 \cdot 10^{-6}$ and $4.8 \cdot 10^{-5}$ cm s^{-1} respectively, while the corresponding values for the sputtered LiPON

- Li_xCoO_2 solid-solid interface were $1.2 \cdot 10^{-7}$ and $6.7 \cdot 10^{-8}$ cm s^{-1}, respectively. These provide an effective comparison respective to carbon graphite, $k^o = 3.0 \cdot 10^{-7}$, $Li_xMn_2O_4$ where $k^o = 5.5 \cdot 10^{-8}$, and Li_xTiO_2 (Anatase) where $k^o = 2.6 \cdot 10^{-10}$. We further use the method of Nicholson and EIS to assess the quality of and changes in kinetics between a common room temperature ionic liquid, BMIM-TFSI, and its quasi-solid porous *ionogel* counterpart, while indicating the shortcomings of the earlier explored DPS method for high-rate interface kinetics. Variations in kinetic parameters are attributed to the effects of confinement within the porous ionogel network at 11 and 8 nm average pore size, producing a reduction in the diffusion coefficient of 70 percent, and a reduction in the heterogeneous interfacial kinetics of 56 percent.

The thesis of Nicholas Abraham Ware is approved.

Jane Pei-Chen Chang

Chong Liu

Bruce S. Dunn, Committee Chair

University of California, Los Angeles

2021

Dedication Page

My work is dedicated to my parents, Gary Ware and Greta Sholachman, and the love of my life, Raphaela McIntyre-Morton. This is for my great-grandparents as well, whose wisdom in crisis saved our entire family and brought us from Poland, and Russia, to the United States before the start of WWII. I owe you everything.

I further dedicate my work to the people and the creatures of this world. May we survive these difficult times and thrive.

Table of Contents

List of Figures

List of Tables

1. Introduction

Solid-state batteries (SSB) have gained traction in literature and adoption in niche commercial sectors, as garnet oxide and sulfide-based solid-state electrolytes (SSEs) have recently shown superionic conductivities matching and exceeding the magnitude of traditional lithium ion battery liquid electrolytes.[1–5] In addition to the promise of safe, nonvolatile lithium ion battery electrolytes, SSEs promise higher energy density due to extended electrochemical voltage windows, as well as the ability to compatibly reintroduce lithium metal as a high energy and high power-density anode without the issues associated with dendrite growth.

The solid-state redox interface plays a critical role in these SSB systems, as it has been found that the solid-solid interface is rate limiting for many of these architectures.[1,6,7] However, a quantitative understanding of the electrochemical (EC) quality of these solid-solid battery interfaces is lacking in the literature, making direct correlation of interface-quality to relative performance difficult. Furthermore, obtaining meaningful quantitative metrics at solid-solid interfaces in SSBs is challenging due to the inherent architecture, in which in many configurations require an additional conductive material to be layered onto the far-end of the solid electrolyte to complete the EC circuit – but unintentionally adding a new solid-solid interface (as indicated in Figure 1), which is likely to impact the measurement. As a result, any all-solid-state electrochemical measurements are confounded by the presence of a multiplicity of interfaces, and an inability to deconvolute one interface from another. Accordingly, it is necessary to develop a technique in which all interfaces, with the exception of a single primary interface, possess negligible interfacial resistance along with overwhelmingly strong kinetics relative to the primary interface of interest.

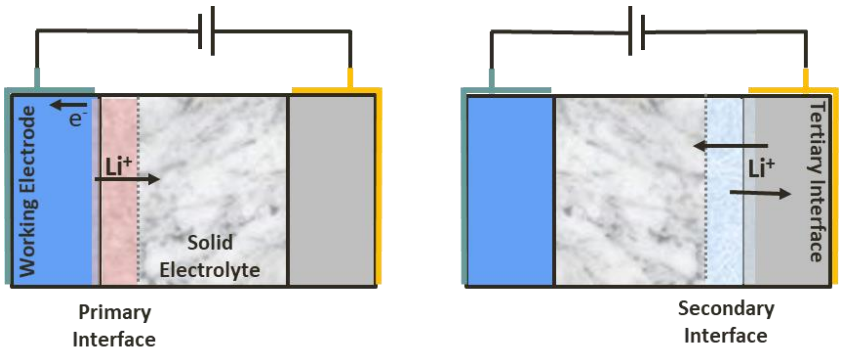

Figure 1: Diagram of unintentionally added interfaces present in all-solid-state test geometries. At left the (non-specific) primary interface under investigation is shown where the working electrode contacts the solid electrolyte. The non-blocking, semi-infinite lithium source counter electrode (grey) generates an unintended secondary interface at the solid electrolyte. Additional tertiary interfaces may also be generated when depositing the current collector on top of the counter electrode. Typical sources of non-primary, complicating interfaces include poor adhesion, temperature effects upon the chemistry, void formation, and any inhomogeneity from the processing and application of the counter electrode and final current collector. A similar set of schematics may be seen in "Interface Stability in Solid-State Batteries" by Gerbrand Ceder, *et. al.*[16]

Thin film lithium cobalt oxide (Li_xCoO_2 or LCO) is an ideal model system in which to evaluate electrochemical interface kinetics as it provides a thoroughly studied lithium intercalation system which is free of binder and is defined by the pure LCO properties. Furthermore, Li_xCoO_2 is among the more prominent and commercially available cathode materials.[8–13] Likewise, amorphous lithium phosphorus oxynitride (LiPON) is among the most intensively studied solid electrolyte materials and is now in use in commercially available thin film solid-state battery (TF-SSB) system, utilized by companies such as Cymbet, Front Edge Technology, and Bolloré.[14] Prior studies in the literature have provided needed insights on the impact of solid-electrolyte properties on device performance, such as minimum possible thickness,[15–17] effects of intentional addition of interphase layers,[2,7] and the impact of thermal treatments.[18,19] However, at this time strides still need to be made in establishing a quantitative analytical technique to effectively decouple simultaneous EC processes in SSB systems and characterize the solid-state electrolyte/solid electrode (SSE/SE) interface kinetics. This work aims

to present such a strategy which should be widely applicable to obtain quantitative kinetic assessment of solid-electrolyte charge-transfer interfaces.

The work in parts I and II of this thesis present a chronocoulometric potential step methodology to investigate solid-state electrolyte/solid electrode interfaces, probing the fundamental and quantitative electrochemical attributes of half-cell thin film solid-state batteries and equivalent architectures. We intend to elucidate the changes in reaction rate at the interface of $LiCoO_2$ as the cathode material goes from contact with a wetting liquid electrolyte, to an SSE/SE interface using both sputtered and ALD-deposited LiPON solid electrolyte. In part II, the changes in reaction kinetics between a bulk ionic liquid electrolyte and the quasi-solid porous silica electrolyte (hereto called an ionogel) are investigated, aiming to understand the effects of electrolyte confinement in a microporous aerogel system. It is hypothesized that there will be no reduction in rate kinetics for electron charge transfer at the interface, as the quasi-solid ionogel electrolyte is fully wetting at the platinum current collecting surface despite the solid silica network that retains ionic liquid electrolyte through capillary force – making the ionogel interface highly analogous to the pure liquid interface.

Figure 2 shows diagrammatically the half-cell configuration in which liquid electrolyte forms an ion exchange interface with the solid or quasi-solid (ionogel) electrolyte, allowing the charge transfer species (Li^+ or ferrocene for sections I and II, respectively) to be transported through a solid or quasi-solid film and perform electron transfer at the interface. In section I, we propose and show evidence that the PC-$LiClO_4$/LiPON interface is nonreactive and nonlimiting to the system, thus providing the opportunity to directly measure the electrochemical properties and kinetics of the $LiCoO_2$/LiPON interface. We plan to show that this methodology can be

extended to a wide-range of solid-solid electrolyte/electrode architectures in which the solid-electrolyte/liquid-electrolyte systems are stable.

2. Analysis of the Solid-Solid Interface, Extrapolated for the $LiCoO_2$ – LiPON System

2.1. LCO – LiPON Solid-State Batteries

The lithium cobalt oxide cathode and LiPON solid-state electrolyte systems have each been widely studied with a great degree of interest being focused onto the phenomena occurring at the interface of electrode and electrolyte. Investigations of interdiffusion,[20–22] formation of resistive inter-phase layers,[23] and deposition of artificial interface coatings to reduce interfacial reactions and enhance ion transport,[7,19,24,25] all deal with the importance and efforts to mitigate interface reactions occurring at the LiPON-$LiCoO_2$ interface and common to solid electrode-solid electrolyte architectures.

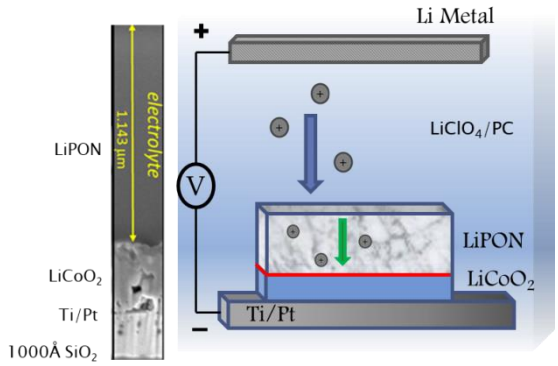

Figure 2: Configuration of the LiCoO2/LiPON as submerged in liquid electrolyte half-cell. At left is shown an SEM image of a microtome sample, indicating 1.143µm LiPON film atop approximately 400nm LiCoO2/Pt/Ti/SiO2/Si. The primary interface is shown in red.

As seen in Figure 2, samples of LCO/LiPON were immersed in lithium perchlorate/propylene carbonate liquid electrolyte, and analyzed in a 3-neck half-cell configuration with lithium counter and reference electrodes. This configuration is significant, as it allows only a single interface in the entire system to dominate: the interface of the LiPON film

deposited onto sputtered thin film $LiCoO_2$ cathode. The other interfaces involved, namely lithium in contact with $LiClO_4$/PC and the LiPON-liquid electrolyte interface, have been found to be nonreactive and very low impedance even over long exposure.[17,27] The $LiCoO_2$ thin films electrode used in this work is found by RAMAN analysis to be of "high temperature" crystalline quality (Figure 3), and the morphology of the sputter deposited structure of SiO_2/Ti/Pt/$LiCoO_2$/LiPON is consistent with literature as can be seen in Figure 4.[8,18,26] Formation of thee LCO crystal structure is dependent upon the deposition or synthesis processes, and most specifically on the crystallization temperature or any post annealing process. So-called high-temperature lithium cobalt oxide (HT-LCO) forms in the rock salt structure with a layered hexagonal unit cell (a = 2.80 Å, c = 14.08 Å) with rhombohedral R3m space group designation, most commonly synthesized with a post-anneal process near 700 C. The low-temperature (LT-LCO) phase forms when crystallized at temperatures below 400 C, and takes on a partially disordered rock salt structure (a = c = 7.08 Å) with a cubic Fd3m space group designation. For the HT-LCO lattice, lithium and cobalt ions reside in alternate layer octahedral sites, while in LT-LCO the octahedral sites are partially disordered with ¼ lithium ions in the cobalt layer and ¼ cobalt ions found in the lithium layer.[9-13,18,80]

Stability of the LiPON/$LiClO_4$-PC electrolyte is noted in the literature, and is validated in this work by the stable open circuit voltage (OCV) and electrochemical impedance (EIS) over a 48 hour $LiClO_4$-PC soak (Figure 5).[17,27,28] It should be noted that the OCV does not fully stabilize to a zero slope here because of the "holding-current" being applied automatically by the potentiostat during the intermittent electrochemical impedance measurements, causing the stabilization period to be longer than otherwise expected.

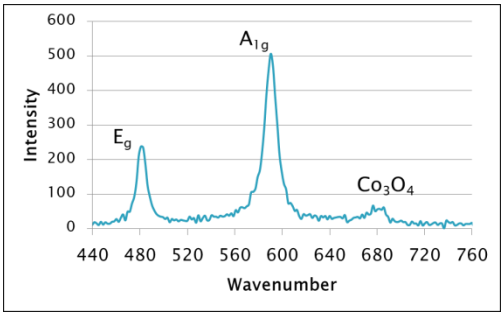

Figure 3 RAMAN profile for $LiCoO_2$, showing expected A_{1g} and E_g peaks typical of high quality, so called "high temperature" polycrystalline $LiCoO_2$.

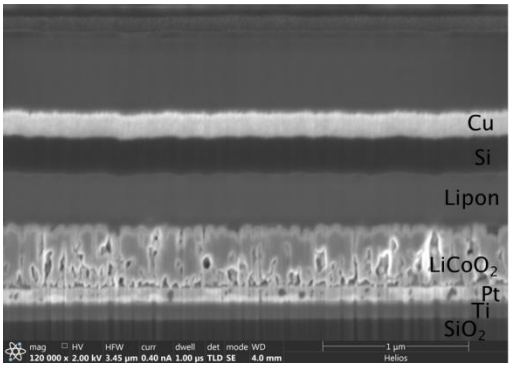

Figure 4: SEM image showing deposited LCO and LiPON on SiO_2/Ti/Pt, in this case in a full-cell configuration which includes e-beam deposited Si and Cu at the top of the structure (Si and Cu structure not relevant in this work).

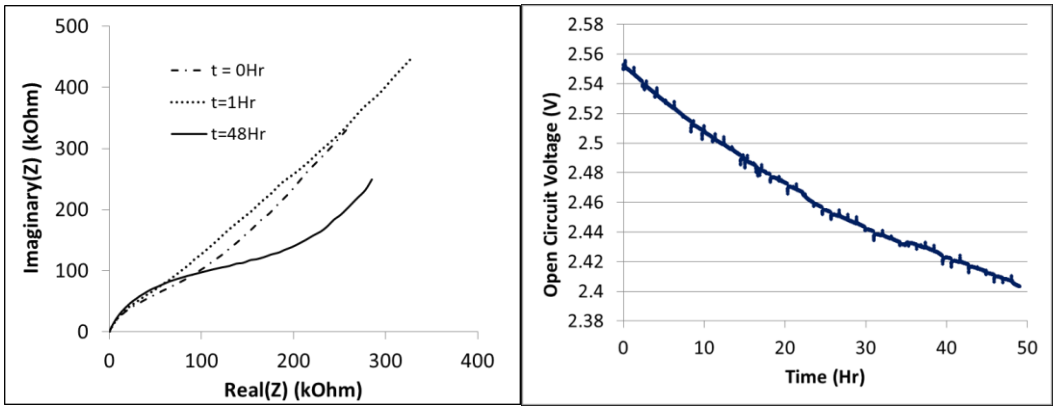

Figure 5: (Left) Measurement of the EIS profile for LiPON deposited directly onto Si/Ti/Pt substrate, allowed to soak in $LiClO_4$-PC liquid electrolyte over 48 hours, indicating no formation of additional reaction layer. (Right) Open circuit potential of the Ti/Pt/LiPON specimen measured over 48 hours between intermittent EIS scans, indicating only nominal changes in chemical potential vs Li, suggesting interface stability between solid and liquid electrolyte.

2.2. Techniques and Methods

2.2.1. Materials

Anhydrous propylene carbonate (Sigma Aldrich, 99.70% purity, <0.002% H2O) and lithium perchlorate salt (Sigma Aldrich, battery grade, 99.99%) were stored in an Argon glovebox with moisture and oxygen content maintained below 1 ppm. Chemicals were used without further purification.

2.2.2 Electrode preparation

Methods for fabrication have been described elsewhere[15,73,74] Briefly, samples were fabricated on Si (001) substrate with a 100 nm silicon dioxide insulating layer. 20 nm titanium and 120 nm platinum thin film were sputtered for adhesion and current collector, respectively, followed by 450 nm $LiCoO_2$ cathode from a 3" target without exposure to air. Annealing was then performed at 700 °C in ambient under oxygen flow for 2 hours to form the high-temperature phase, as verified by Raman spectroscopy. Following heat treatment, relevant samples were replaced in the sputter chamber and 1.1 µm Lipon solid electrolyte was deposited from 3" LiPO target under N_2 flow.

ALD Lipon was deposited onto the above $LiCoO_2$ cathode via the process described by Pearse, Rubloff, et al. elsewhere.[72]

Prior to use in the below described electrochemical testing apparatus, chemically resistive biaxially-oriented polyethylene terephthalate (BoPET) tape was used to mask off the reverse side of all specimen, eliminating the possibility for electrochemical response from the silicon substrate. BoPET was additionally used to mask a small space including a portion of the platinum

shelf and the upper-most portion of $LiCoO_2$ or $LiCoO_2$/Lipon, in order to more precisely control the exposed surface area of the active electrode material.

2.2.3. Methods

A BioLogic VMP3 multichannel potentiostat was used to carry out galvanostatic cycling, cyclic voltammetry, double pulse chronoamperometry and electrochemical impedance spectroscopy (EIS). Electrochemical measurements were performed in an argon glove box with moisture and oxygen levels maintained at < 1ppm. Thin film Li_xCoO_2 as well as Li_xCoO_2 coated with LiPON solid electrolyte were evaluated using a 3-neck flooded cell with 1M $LiClO_4$ in Propylene Carbonate (PC), using lithium metal as counter and reference electrodes.

EIS was collected at room temperature inside the argon glovebox using a frequency range of 1MHz to 100mHz with 10mV amplitude, omitting frequency regimes where inductance from the contacts and wires obstructed specimen data. Galvanostatic cycling between chronoamperometry measurements was carried out at ca. C/2 rate unless otherwise specified.

Samples of LCO/LiPON were submerged to below the platinum contact shelf in lithium perchlorate/propylene carbonate liquid electrolyte, and analyzed in a 3-neck half-cell configuration with lithium counter and reference electrodes. This configuration is significant, as it allows only a single interface in the entire system to dominate: the interface of the LiPON film deposited onto sputtered thin film $LiCoO_2$ cathode. The other interfaces involved, namely lithium in contact with $LiClO_4$/PC and the LiPON-liquid electrolyte interface, have been found to be nonreactive and very low impedance even over long exposure.[17]

2.3. Heterogeneous Rate Constant – Background

Through the data presented below and as expected, it is clear that solid electrolyte-solid electrode interfacial ion transport kinetics presented here are sluggish compared to the equivalent liquid electrolyte system. Conjecture may be made on a broad range of causes for this result, including: imperfect interface "contact wetting" in terms of structural access for ion transfer at the solid-solid interface (i.e. voids and porosity), versus that of the liquid-solid interface; interdiffusion and local lithium migration between $LiCoO_2$ and LiPON during deposition, annealing, and early cycling[20,29] creating a stoichiometrically mixed and resistive interlayer; lower bulk diffusion for sputtered and ALD LiPON relative to liquid PC-$LiClO_4$ leading to changes in the mobile-species concentration gradient and reduced ion or reaction site supply at the kinetic interface; and potential for increased structural and atomic configuration energy costs for reorganization per Marcus Theory. From the theory of Marcus,[30,31] the heterogeneous standard rate constant (HRC) is a quantitative expression of the energy required to reconfigure local atomic geometry for a chemical species directly prior to electron transfer, as well as any reconfiguration occurring in the local solvation shell. While determination of the extent and atomic nature of the above discussed physical, chemical and solvation interface changes is left to other characterization approaches, assessment of the heterogeneous rate constant is of paramount value to understanding the quality of battery-material interfaces, irrespective of the cause of any interfacial or local species changes.

2.4 Chronocoulometric Assessment of Heterogeneous Rate Constant

For double potential step chronocoulometry (DPSC) techniques, the electrode is initially equilibrated at a potential state at which no anodic or cathodic redox current flows. For anodic

formal rate constant measurements, the $LiCoO_2$ is equilibrated by a potential hold below 3.65 V (all potentials measured versus lithium unless otherwise specified) until the current recedes below approximately 1 µA cm^{-2}, while for cathodic measurements the equivalent process is carried out at 4.15 V. Between the two measurements, a full galvanostatic charge and discharge cycle is carried out, leading to the next cycle of equilibration at the redox-inactive region. In using the DPSC process to assess the formal heterogeneous rate constant, the voltage is stepped from the equilibrated potential to the formal potential or other desired potential at which we expect redox to occur (Figure 6), held for 5 seconds, and then returned to the original potential. Data points were recorded every 10 ms or every 1 µA.

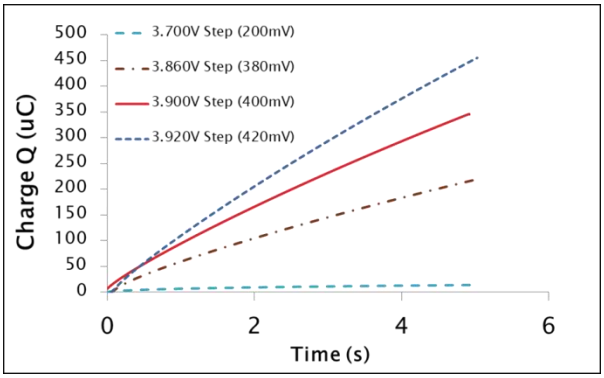

Figure 6: Charge versus time during DPSC over 5 seconds of the potential jump into faradaically active region, from the redox inactive region below 3.50V vs Li, indicating sequentially larger redox activity for larger potential steps as expected.

The kinetic current response to a potential step is analyzed using the theory detailed previously by Christie et al.[32,51,52] and Michael Sharp.[33] High concentration of mobile lithium in the electrode and in the solid and liquid electrolytes allow the charge storage contributions of adsorbed ions and double layer buildup to be ignored when analyzing the total charge passed upon DPSC. Convection effects may be ignored for the flooded cell using sufficiently small currents.[34] For a potential step which sufficiently favors the cathodic reduction response such

that the cathodic current far outweighs the anodic current (i.e. $i_c >> i_a$), the charge component for the total response can be described by

$$Q = Q_d = nFAD_{Ox}{}^{1/2}C_{Ox}\left(\frac{2}{\sqrt{\pi}}t^{1/2} - \frac{1}{\lambda}\right), \quad (1)$$

where C_{ox} is the bulk concentration of the oxidized reaction species, A is the active electrode surface area, and λ as described in Eq. 1 is a constant which is dependent on the formal rate constant, the cathodic transfer coefficient, and the formal overpotential ($E-E^o$). It can be seen that at sufficiently long times where $2t^{1/2}/\sqrt{\pi} >> 1/\lambda$, then $\partial Q/\partial t^{1/2}$ becomes a constant and the faradaic response is diffusion controlled.

When the Q vs $t^{1/2}$ plot becomes linear at sufficiently large $t^{1/2}$ (Figures 7(b), (d), and (f)), the total charge passed and the resultant limit of the slope is expressed as:

$$Q]_{asym} = \frac{2K}{\lambda\sqrt{\pi}}t^{1/2} - \frac{K}{\lambda^2} \quad (2)$$

$$\frac{\partial Q}{\partial t^{1/2}}\Big]_{lim} = \frac{2K}{\lambda\sqrt{\pi}} \quad (3)$$

$$\text{where } K = nFAk^oC_{Ox}exp\left(\frac{-\alpha nF(E-E^o)}{RT}\right) \quad (4)$$

K is a Butler-Volmer expression for the cathodic current in the absence of adsorption or concentration polarization, and has units of Amperes when concentration is expressed in mol cm^{-3}.

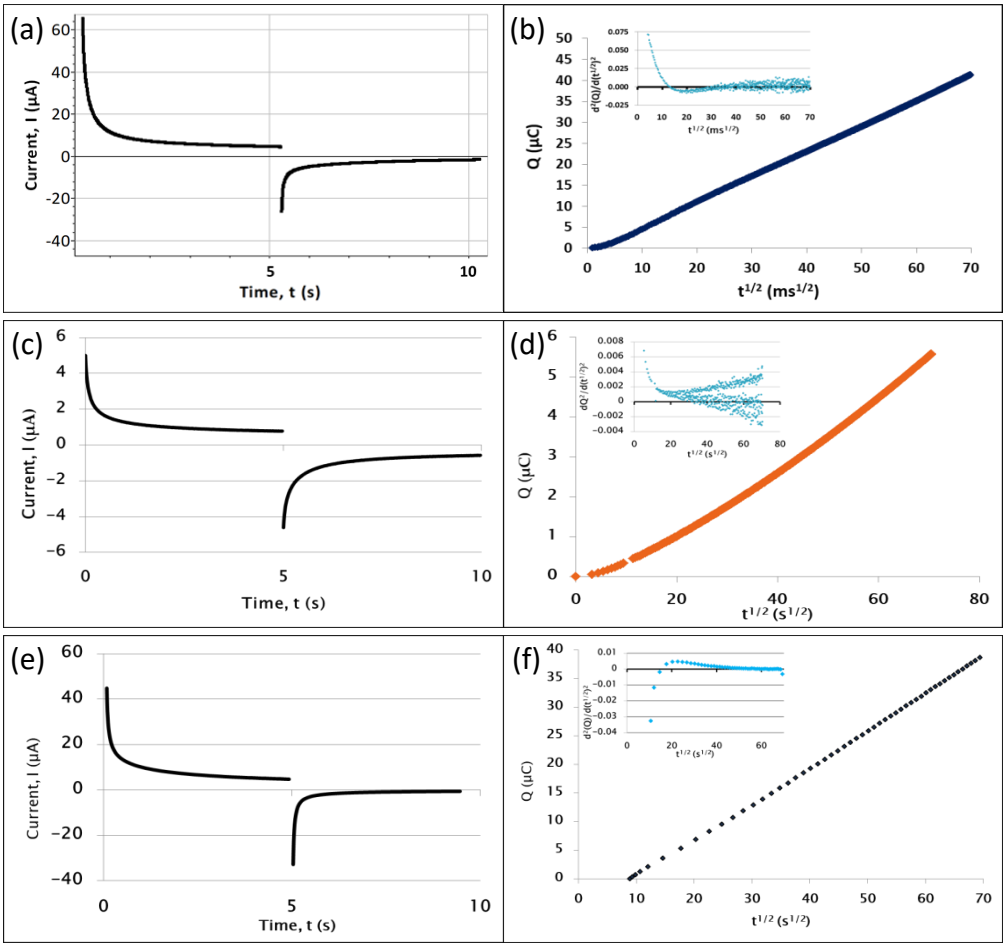

Figure 7: (a) Current transients for a double potential step, from 3.4V to 3.9V and back, for bare thin film $LiCoO_2$ in liquid PC-$LiClO_4$ electrolyte. (b) Initial anodic potential step producing Q vs $t^{1/2}$ with linearization clearly evident where the 2nd derivative (inset) centers around zero. (c) Current transients for a double potential step, from 3.4V to 3.9V and back, for 1.1um sputtered LiPON on $LiCoO_2$ in liquid PC-$LiClO_4$ electrolyte. (d) Initial anodic potential step producing Q vs $t^{1/2}$ with linearization clearly evident where the 2nd derivative (inset) centers around zero. (e) Current transients for anodic double potential step from 3.4V to 3.9V and back, for 40nm ALD LiPON on $LiCoO_2$ in liquid PC-$LiClO_4$ electrolyte. (f) Initial anodic potential step producing Q vs $t^{1/2}$ with linearization clearly evident where the 2nd derivative (inset) centers around zero.

In order to establish a kinetic relationship to the steady-state asymptotic behavior of Q vs $t^{1/2}$, the slope is extrapolated to Q = 0 where the transient is otherwise nonlinear at small times, providing the intercept $t_i^{1/2}$. Determining the intercept from Eq. 3 and substituting back into Eq. 2 yields the relationship for the cathodic current in terms of the kinetic parameters (Eq. 6).

$$\frac{2t_i^{1/2}}{\sqrt{\pi}} = \frac{1}{\lambda} \tag{5}$$

$$K = i_c = \frac{\pi \cdot \left(\frac{\partial Q}{\partial t^{1/2}}\right)}{4 t_i^{1/2}} \quad (6)$$

The formal heterogeneous rate constant, k_f^o, can now be measured in the cathodic regime by performing a DPS to the formal potential:

$$k_f^o = \frac{i_c(E=E^o)}{nFAC_{Ox}} \quad (7)$$

It must also be recognized that the value of the heterogeneous rate constant is an "apparent" value, based on the impacts that the electrical double layer at the electrode surface has on the value of k_f^o, which are exceedingly difficult to measure for solid electrodes.[33] Therefore, all measurements are assumed to be valid for only the apparent heterogeneous rate constant, k_f^o (app), which is the typical value reported in literature for different methods of determining of the values of the formal heterogeneous rate constants.

2.5. Results

Tabulated values of the apparent heterogeneous rate constant, k_f^o(app), are given in Table 1 and represented visually in Figure 8. In addition, the values from this work are compared to the rate constants of other insertion materials found in literature in Table 2. For bare $LiCoO_2$ samples in contact with propylene carbonate/lithium perchlorate organic electrolyte, k^o(app), the apparent anodic formal rate constant is measured at 1.15 x10^{-6} cm s^{-1} describing deintercalation at the $LiCoO_2$ interface from the fully intercalated state, while the kinetics for cathodic exchange were measured at 4.83 x10^{-5} cm s^{-1}. It is of interest to note that the process of electrochemical exchange at the interface is more than an order of magnitude higher for the process of ion insertion into the $LiCoO_2$ lattice from the solvated state, versus that for the deinsertion process from solid into liquid. Sputtered LiPON electrolyte films of 1.1 µm on $LiCoO_2$

films registered 1.20 x10^{-7} cm s^{-1} and 6.70 x10^{-8} cm s^{-1} respectively for apparent anodic and cathodic formal rate constants. Meanwhile, 40 nm thick LiPON films deposited via the ALD process produced apparent formal heterogeneous rate constants of 4.86 x10^{-7} cm s^{-1} and 7.46 x10^{-8} cm s^{-1} respectively for anodic and cathodic redox processes. Continuing work by this author aims to show that the k^o values determined by DPSC in the insulating and near-insulating potential range of LCO do not change in correlation with the R_{CT} values determined by EIS, and in fact are similar to the kinetics effective near the formal potential and in the conducting region.

	Bare $LiCoO_2$ PC-$LiClO_4$	1.1µm Sputtered Lipon	40nm ALD Lipon
Anodic k_f^o (app) (cm s^{-1})	$(1.15\pm0.47)\cdot10^{-6}$	$1.20\cdot10^{-7}$	$4.86\cdot10^{-7}$
Cathodic k_b^o (app) (cm s^{-1})	$(4.83\pm1.23)\cdot10^{-5}$	$(6.70\pm0.30)\cdot10^{-8}$	$7.46\cdot10^{-8}$

Table 1: Results of the determination of the heterogeneous rate constant for the LCO electrode interface with liquid and solid electrolyte interfaces.

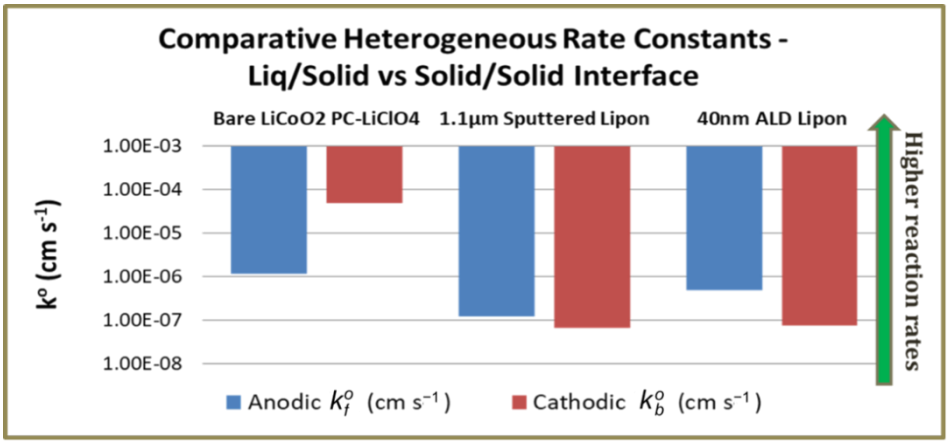

Figure 8: Visual representation of the kinetic rate constant results from Table 1.

	Carbon Graphite[a]	$LiCoO_2$	1.1 um LiPON-$LiCoO_2$	ALD LiPON-$LiCoO_2$	$LiMn_2O_4$[b]	TiO_2 Anatase[c]
k^o_s (app) (cm/s)	3.0 to 5.4 E-7	2.5 E-5	9.4 E-8	2.8 E-7	5.5 E-8	2.6 to 5.5 E-10

Table 2: Comparison of values for the heterogeneous rate constants determined in this work relative to those for other battery materials in literature, each evaluated relative to their respective liquid electrolyte systems. Citations a, b and c refer to references 40, 41 and 42, respectively.[40–42]

Current responses of all three interfacial architectures are shown in Figure 7(a, c, e), and the linearization of the steady state region, as defined by Eqs. 2-4, is seen in Figure 7(b, d, f). Using DPSC and relating i_c from Eq. 6 to the relative size of the step potential ($E\text{-}E^o$) as seen in Figure 9, we further determined the value of the cathodic transfer coefficient, α, to be 0.68 for bare-$LiCoO_2$ thin film in $LiClO_4$. To the authors' knowledge, this is the first report of an empirical determination of this kinetic parameter for lithium cobalt oxide, though it has been estimated at 0.5 for modeling parameter selection purposes in a few noted works without justification.[35,36] The relationship between i_c and ($E\text{-}E^o$) follows Eq. 8 from Sharp et al., as expressed below:[33]

$$i_c = n\mathrm{F}AC_{\mathrm{ox}}k_f^o exp\left(\frac{(1-\alpha)n\mathrm{F}(E-E^O)}{RT}\right) \quad (8)$$

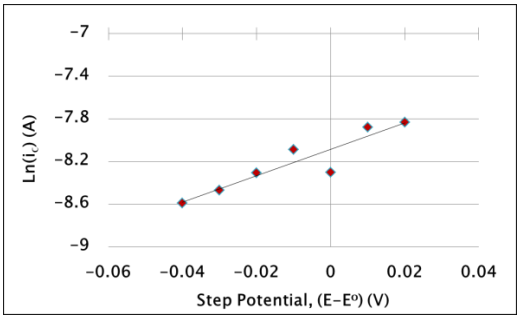

Figure 9: Ln(i_a) vs Step Potential for Bare-$LiCoO_2$ used for the determination of the cathodic transfer coefficient, in this case determined as α = 0.68.

For battery materials, the predominant method of interfacial kinetic analysis – along with numerous other electrochemical applications – is electrochemical impedance spectroscopy. Depending on the material system and the AC impedance response, values such as the diffusion coefficient, bulk conductivity, uncompensated resistance, and charge transfer resistance are routinely obtained by applying an appropriate equivalent circuit and modeling the impedance profile via specialized software. Charge transfer resistance (R_{CT}) is a measure of the energy required for electron transfer to oxidize or reduce an electrochemical species at a phase

boundary (e.g., liquid-solid or solid-solid boundary), and gives a relative representation of the rate at which the electron transfer can take place. By assuming that the small AC perturbations from EIS are representative of faradaic activity near equilibrium (E_{eq}), the charge transfer resistance can be related to the exchange current (i_0). Once the exchange current is determined, the heterogeneous rate constant is obtained via the following relationships (Bard and Faulkner, Ch. 3):[34]

$$R_{CT} = \frac{RT}{nFi_0} \tag{9}$$

$$i_0 = FAk^o C_{Ox}^* e^{-\alpha f(E_{eq}-E^o)} \tag{10}$$

$$R_{CT} \sim {}^{1}/_{k^o} \tag{11}$$

Here, R_{CT} is the charge transfer resistance determined by an equivalent circuit model, i_o is the exchange current, C_{ox} is the concentration of the oxidized species, F is the Faraday Constant, and f = F/RT. If we take the conversion of R_{CT} to k^o (discussed earlier) as an accurate assessment of the reaction kinetics at the material system's CT interface, we should expect to see a logically consistent trend between the HRC derived from DPSC, and the charge transfer resistance determined by EIS.

It is well understood that for the lithium cobalt oxide electrode in organic liquid electrolyte, charge transfer resistance as measured by EIS shrinks greatly dependent upon delithiation (shown both in the impedance profiles of Figure 10, and the galvanostatic charge derivative in Figure 11), concurrent with an insulator-to-conductor Mott transition which enables facile charge transfer at higher potential.[10,37] Measurement of the formal heterogeneous rate constant for $LiCoO_2$ in liquid PC-$LiClO_4$ electrolyte via DPSC in this work validates that the interfacial ion exchange kinetics are greatly improved for cathodic re-lithiation in the conducting

Li_xCoO_2 state, versus k_o of the anodic charge transfer from the insulating state of Li_xCoO_2. Indeed, it is not possible to reliably obtain a value for R_{CT}, and therefore the associated k_o value as derived above, at low potentials of Li_xCoO_2 near x = 1 (i.e. 3.7 V) as the charge transfer semicircle at mid-frequencies has not matured and cannot be effectively distinguished from the capacitive and diffusive elements that dominate in this regime (Figure 10). Impedance models are thus seen to have their limitation in providing a comprehensive understanding of a material system and the accompanying behavior throughout its entire active potential range.

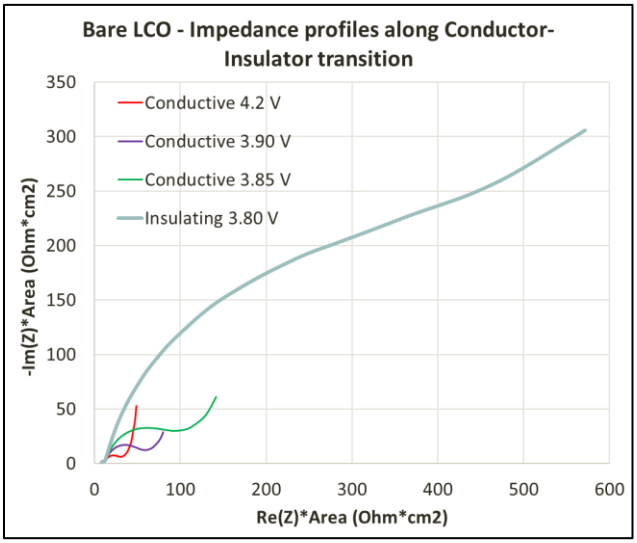

Figure 10: Mapping of the general charge transfer resistance depressed semicircle (see: figures 12-15) in the electrochemical impedance spectroscopy of Bare-LCO in liquid electrolyte, $LiClO_4$-PC, for intermediate potentials in the active intercalation/deintercalation region where R_{CT} and associated mixed conductivity undergoes the Mott metal-to-insulator transition.

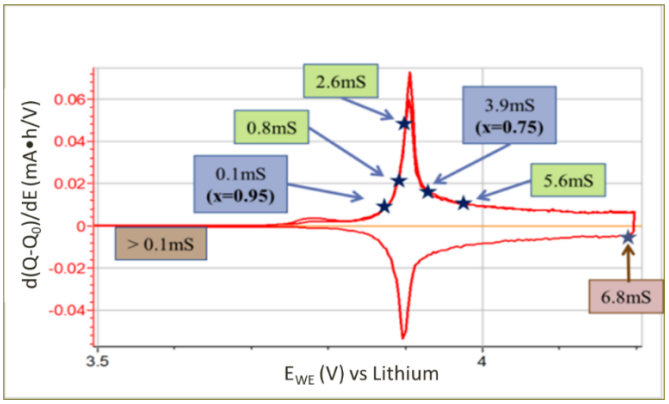

Figure 11: Mixed-conductivity map superimposed onto the galvanostatic derivative curves of Li_xCoO_2 showing coincidence of the Mott insulator-to-metal transition with the intercalation behavior.

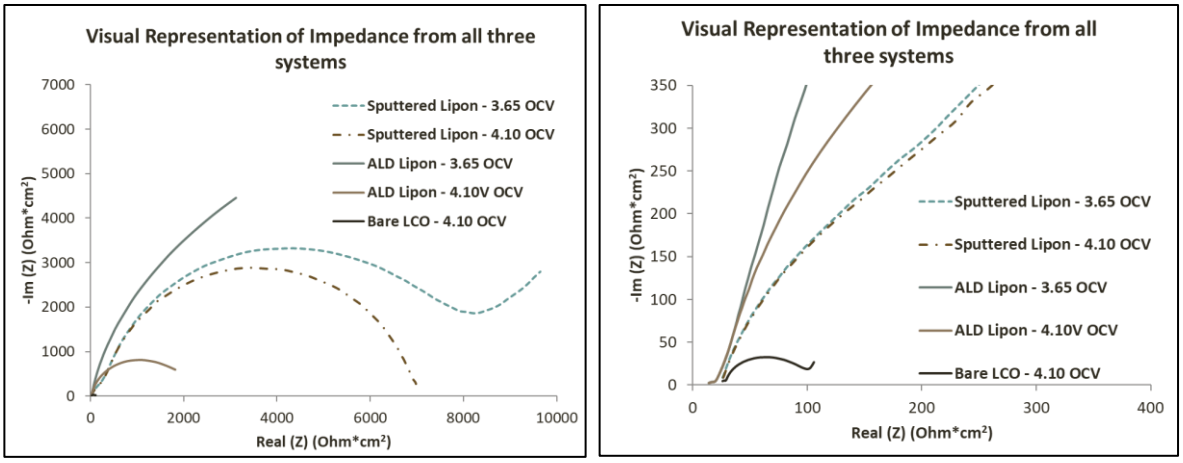

Figure 12: Electrochemical impedance spectroscopy taken for sputtered and ALD LiPON on LCO as compared to that of bare-LCO, each in $LiClO_4$-PC liquid electrolyte. Right-hand figure presents the same data, focused near |Z|=0.

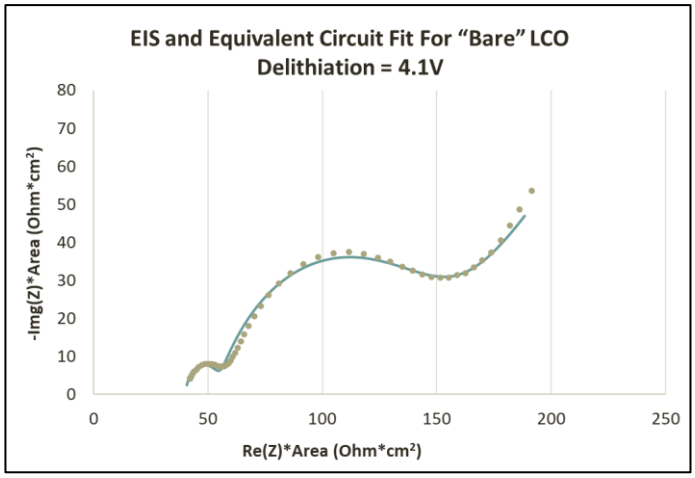

zFit Model: Bare LCO at 4.1 V		
R_{Series}	40.4	$\Omega \cdot cm^2$
Q_2	0.719 e-6	$F \cdot s^{(a-1)} \cdot cm^2$
a_2	0.990	-
$R_{2\ LCO\text{-}Surface\ Film}$	13.3	$\Omega \cdot cm^2$
Q_3	0.132 e-5	$F \cdot s^{(a-1)} \cdot cm^2$
a_3	0.7461	-
$R_{3\ CT}$	100.2	$\Omega \cdot cm^2$
W_3 (aka s_3)	97.8	$\Omega \cdot s^{-1/2} \cdot cm^2$

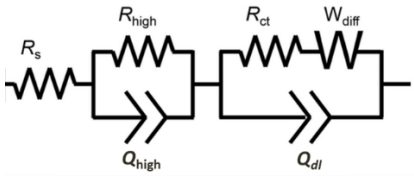

Figure 13: (Left) Fitted (line) equivalent circuit model of Bare-$LiCoO_2$, measured (circles) in $LiClO_4$-PC. The equivalent circuit equation is $R_1+Q_2/R_2+Q_3/(R_3+W_3)$ where R is a resistance element, Q the constant phase element, and W the Warburg diffusion element. The X^2 value for this fit is sufficiently precise at $X^2/|Z| = 2.21 \cdot E\text{-}2$. (Right) The values of the fitted impedance profile. (Bottom) The transmission line equivalent circuit model used and detailed for "Bare LCO" electrochemistry, as well as for LiPON-on-LCO electrochemistry.

EIS equivalent circuits, such as that seen in figure 13, model electrochemical systems using typical circuit elements such as resistors (R), capacitors (C), and inductors (I), along with more complex modeling components such as constant phase elements (Q) and Warburg diffusion elements (W). Briefly, constant phase elements (CPEs) act in likeness to true capacitors but have

a phase angle that is independent of the signal frequency. These equivalent circuits model processes occurring within an electrochemical system, such as the electric double layer capacitance along certain phase boundaries within a battery material, ionic and electronic resistances to current, and long-range diffusion processes through the electrodes and electrolytes.

The equivalent circuit model is most often shown in relation to the true system response along a Nyquist plot, also known as the complex impedance plane, along with a fitting parameter $X^2/|Z|$, which should be as small as possible and denotes the least-squares difference between model and empirical results. Figures 13-15 show the model (line) and empirical (circle) data along a Nyquist plot – including the circuit-element value parameters – for the bare-LCO, LCO-sputtered LiPON, and LCO-ALD LiPON systems respectively, in PC-$LiClO_4$. For each system, the meaning of each circuit element is labeled in the subscript text, is directly related to the real electrochemical processes relevant to the particular EC system, and have been validated by authored studies for both the bare LCO and LCO-LiPON systems. The validity and meaning of these equivalent circuit models are further discussed below in the section titled "Validation of Sharp's DPSC Technique for obtaining the HRC."

Regarding the impedance data provided in figure 13, it has been shown[10,56,61] for bare LCO in liquid electrolyte that the first parallel element of the equivalent circuit model ($R_{high}|Q_{high}$) from the same figure may be correctly attributed to the interactions within the native surface film formed at the liquid-solid interface, and may be left off in the aim of solely isolating the charge-transfer resistance. The element parameter value difference between a 2-parallel and a 1-parallel equivalent circuit model (not provided here) is extremely small, with regard to the

charge transfer resistance obtained. Removing the small R-Q parallel circuit from the fitting model removes any trace of fitting for the LCO "surface films" half-circle impedance response. This observation does well to validate the appropriateness and meaning of the 2-parallel-circuits impedance model relative to the nature of the electrochemical reaction in the true material.

The Bode plot illustrated in Figure 14 presents the identical data as its sister Nyquist plot in the same figure using a different set of axes. A Bode impedance plot shows the phase difference (right y-axis) between the applied AC voltage perturbation and the resultant current response, as well as simultaneously representing the log(magnitude) of the impedance (left y-axis) – each versus the log-spaced axis of frequency.

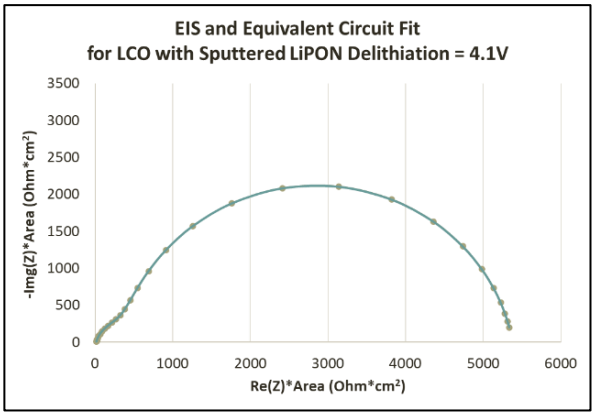

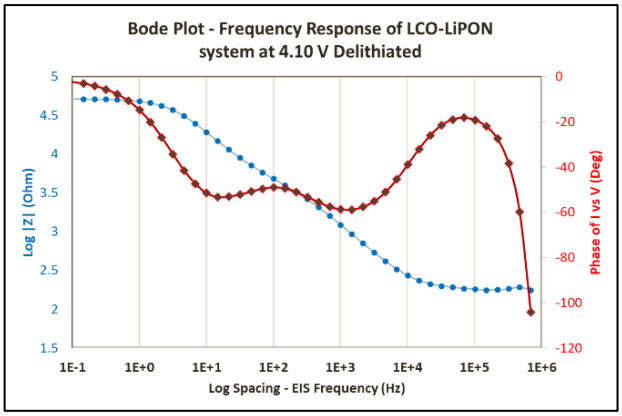

BioLogic EC-Lab zFit Model: 1.1 µm LiPON on LCO, 4.1 V							
R_{Series}	Q_2	a_2	$R_{2\ LiPON\text{-}Bulk}$	Q_3	a_3	$R_{3\ CT}$	W_3 (aka s_3)
16.3	0.854 e-6	0.814	374.5	1.237 e-6	0.889	4,971	1.573
$\Omega \cdot cm^2$	$F \cdot s^{(a-1)} \cdot cm^2$	-	$\Omega \cdot cm^2$	$F \cdot s^{(a-1)} \cdot cm^2$	-	$\Omega \cdot cm^2$	$\Omega \cdot s^{-1/2} \cdot cm^2$

Figure 14: (Left) Fitted (line) equivalent circuit model of sputtered LiPON-$LiCoO_2$, measured (circles) in $LiClO_4$-PC, where the circuit equation is $R_1+Q_2/R_2+Q_3/(R_3+W_3)$. The X^2 value for this fit is sufficiently precise at $X^2/|Z| = 7.37 \cdot E\text{-}3$. (Right) The Bode plot translation of the Nyquist to the left, showing the overall frequency response behavior and two independent processes occurring between 10^0 Hz and 10^4 Hz. (Bottom) The values of the fitted impedance profile, showing the primary charge transfer resistance and indicating a LiPON conductivity of 2.9 E-7 $S \cdot cm^{-1}$.

The charged species in an electrochemical system are limited in mobility by various factors including their ratio of mass to charge, the magnitude of the applied potential, their local

available energy states, along with other factors of their environment. Bode plots are extremely useful in visualizing individual electrochemical responses of the system as certain charged species in their particular environments become capable of oscillation at the instantaneous frequency of the voltage perturbation. As frequency is swept from right to left along the bode plot x-axis (high to low frequency) there are two distinct [sets of] processes which become activated in the areas of 10^1 and 10^4 Hz, as indicated by the two distinct peaks in phase of the response current. These two processes can be understood in correlation with the two distinct semicircles visible in the Nyquest impedance, and pair well with the equivalent circuit model applied: at higher frequency the facile ion conduction in the LiPON electrolyte bulk becomes mobile, while at lower frequencies the charge-transfer process of intercalation (and the associated processes involved in this electrochemical reaction) becomes capable of keeping up with the oscillating AC potential and thus begin to generate AC current. Further, the very high frequency region indicates a large and increasing phase difference near the secondary y-axis; these data points have been left out of the Nyquest plots to avoid incorrect interpretation of the system. This phenomenon may be attributed to inductance in the external wiring and electrical test design architecture, and is typically considered independent of the electrochemical system under study. The overall slope trend of the magnitude of the impedance (i.e., $|Z|$) versus the logarithm of frequency describes the rate of change of the total impedance versus frequency, as more processes become active and acclimate their response to the signal frequency.

For the Warburg impedance in consideration of our physical model, the magnitude and effect of the Warburg is concomitant to the *slowest* diffusion process in the system. Pairing with that, an ensuing capacitance develops upon small local lithium displacements relative to the

partial charges associated with the local stationary cobalt ions at low frequency. Reviewing the second parallel element in our equivalent circuit model (Figure 13), the charge transfer and double-layer capacitance responses have similar time constants and therefore occur in correlation with each other in roughly the same frequency regime.

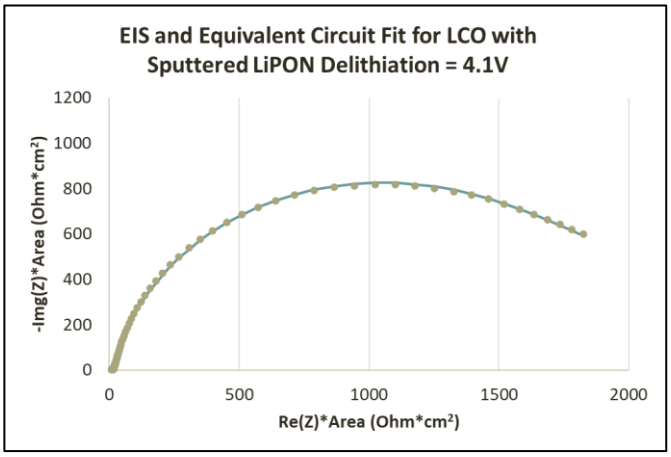

zFit Model: 40nm ALD Lipon on LCO, 4.1 V		
R_{Series}	8.0	$\Omega \cdot cm^2$
Q_2	0.121 e-6	$F \cdot s^{(a-1)} \cdot cm^2$
a_2	1.00	-
$R_{2\ LiPON\text{-}Bulk}$	5.3	$\Omega \cdot cm^2$
Q_3	5.66 e-6	$F \cdot s^{(a-1)} \cdot cm^2$
a_3	0.878	-
$R_{3\ CT}$	1893.3	$\Omega \cdot cm^2$
W_3 (aka s_3)	5004	$\Omega \cdot s^{-1/2} \cdot cm^2$

Figure 15: (Left) Fitted (line) equivalent circuit model of 40 nm ALD LiPON deposited on $LiCoO_2$, measured (circles) in $LiClO_4$-PC. The equivalent circuit equation is $R_1+Q_2/R_2+Q_3/(R_3+W_3)$ where R is a resistance element, Q the constant phase element, and W the Warburg diffusion element. The X^2 value for this fit is sufficiently precise at $X^2/|Z| = 4.26 \cdot E\text{-}1$. (Right) The values of the fitted impedance profile, indicating LiPON conductivity of 7.5 E-7 $S \cdot cm^{-1}$.

In order to validate the diffusion coefficient of the $LiCoO_2$ used in this study relative to published thin-film $LiCoO_2$, we assessed the magnitude of the CV peak current, i_p, in LCO as a function of sweep rate (Figure 16). Using the Randles-Sevcik relation of peak current as a function of the square root of the sweep rate, *v*, we find the magnitude of the diffusion coefficient for the reduced and oxidized species for bare-$LiCoO_2$ in $LiClO_4$-PC to be $1.3 \cdot 10^{-10}$ cm^2 s^{-1} and $1.0 \cdot 10^{-9}$ cm^2 s^{-1}, respectively (Figure 17). These diffusion coefficients are on the higher end of values reported in the literature, which range from 10^{-9} to 10^{-13} cm^2 s^{-1}, with some discrepancy based on the methodology of the analysis.[38,39]

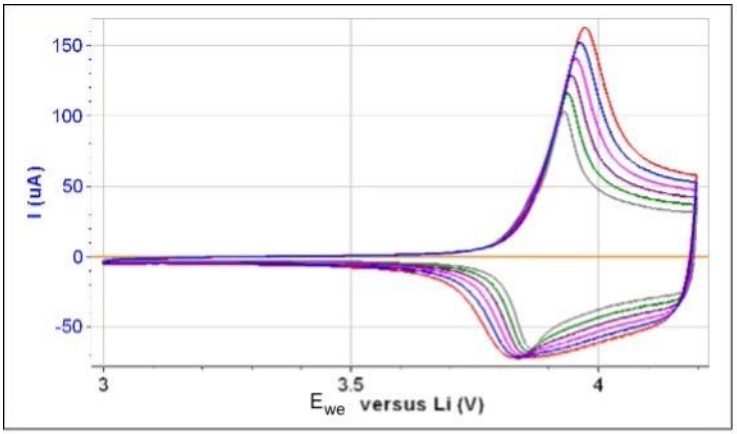

Figure 16: Cyclic voltammetry profiles of bare-LCO in $LiClO_4$-PC liquid electrolyte, showing increasing sweep rates with equal intervals of Δv = 0.2mV s^{-1}, between 1.0 and 2.0 mV s^{-1}. The change in both anodic and cathodic peak current, $i_{p,a}$ and $i_{p,c}$, allows calculation of the diffusion coefficient using the Randles-Sevcik relation.

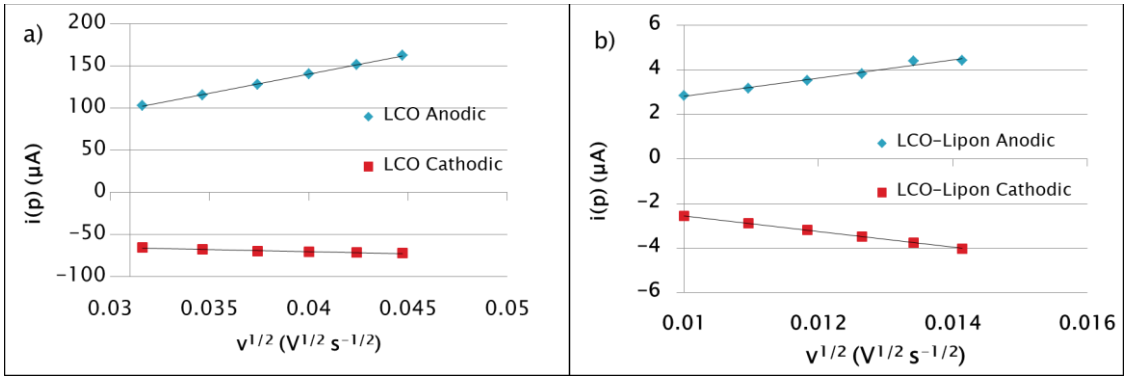

Figure 17: Randles-Sevcik measurement of the diffusion coefficient through the relationship between peak current, i(p), and the square root of the sweep rate, *v*. (a) Slopes for bare-LCO, and (b) slopes for sputtered LiPON solid electrolyte on LCO.

One observation to be drawn from the above data from Table 1 regards the possibility of improved interfacial performance based on the particular deposition method of amorphous LiPON onto thin film $LiCoO_2$. Clearly, in this case, any differences in the contact at the solid-solid interface stemming from the type of deposition are relative to the fundamental electrochemistry of the solid-solid interface, any incurred interdiffusion, thermal treatments, and reconfiguration contributions upon ion transfer. However, equivalence in stability and near-surface stoichiometry in this case reduces the discrepancy between the two systems, while the

methodology may lend itself well to identifying significant improvements from surface treatments or dissimilar electrode-electrolyte pairings on overall charge storage kinetics.

2.6. Validation of Sharp's DPSC Technique for obtaining the HRC

The precise derivation provided by Christie and co-workers from first principles of the relationship between DPSC electrochemistry and the heterogeneous rate constant was first presented in 1964. That publication[32] and Christie et al.'s subsequent related papers[51,52] pertain to the electrochemistry of a two-oxidation-state redox couple dispersed in a liquid electrolyte medium, with electron transfer (ET) occurring at the liquid/current collector interface. In order to establish confidence in the application of the DPSC methodology outlined by Sharp, Christie, Osteryoung and Anson towards finding HRC in a thin-film electrode and a solid-state electrolyte system, it is important to show evidence of agreement versus known and reliable secondary or even tertiary methodologies. Two well-known and widely used methods are applied here to provide evidence of the appropriate application of Sharp and Christie's DPSC approach to obtain the heterogeneous rate constant (relative to the anodic redox kinetics) for the specific architectures tested in this work.

As a comparative standard method, the Nicholson method for obtaining the heterogeneous rate constant is widely used and well understood as evidenced by its being cited 3675 times according to Google Scholar, including 494 citations which involve the key words "lithium ion" and "battery."[53-55] The details and applications of the Nicholson method are further discussed in section 2 of this thesis. Fundamentally, Nicholson developed his electrode reaction kinetics theory based on observing the separation between the anodic and cathodic current peaks during cyclic voltammetry, at a known sweep rate (the rate at which the voltage of the

active “working electrode” increases or decreases relative to the counter electrode). So long as the peak is representative of a single electron exchange between the electrolyte and the electrode, the anodic and cathodic peaks can be used to obtain important information about the reaction kinetics, as well as about the limiting mass transport process occurring in the system. This discussion will not cover the complex mathematics involved in Nicholson’s method as they represent a deep dive into a section of electrochemical theory that is largely not relevant to the present work. One of the primary features lacking in Nicholson’s method, a feature which is directly obtainable through the DPSC method theorized by Sharp and collaborators, is the opportunity to differentiate between intercalation versus deintercalation kinetics as well as obtaining kinetic constants for electrode voltages other than the formal potential. These specific factors in Sharp’s DPSC analysis are desirable for a manifold study of a broad range of secondary battery electrodes.

As a tertiary comparative reference for validating data obtained through DPSC kinetic analyses, Bard and Faulkner[34] detail the mathematics and theory necessary for converting charge transfer resistance (R_{CT}) values from electrochemical impedance spectroscopy (EIS) into values of heterogeneous kinetic rate constants (still measured in cm/s). For EIS, very small perturbations (small amplitude) in the voltage are used over a range of frequencies to drive current in a system, and activate mechanisms that are capable of responding at and below given frequencies. For instance, surface kinetics are typically capable of responding at very high frequencies because their mechanism is the exchange of an electron – a process which can be nearly instantaneous. On the other hand, slow processes such as bulk diffusion are only possible at lower frequencies as they involve a molecule’s random walk through a lattice or a viscous substance, driven by a

[often small] concentration gradient. This small perturbation near an intentionally stabilized equilibrium voltage can be interpreted as a quasi-equilibrium state, allowing the use of analytical electrochemistry to derive characteristic information about our system.

To utilize EIS correctly, the electrochemical redox must be a one-step one-electron process (it should be noted that such an EC standard *must* be true for all techniques described in this thesis to be accurate). For LCO, it is well understood that the intercalation and deintercalation processes involve a cobalt oxidation state transition from Co^{3+} to Co^{4+} for an anodic reaction where cobalt in Li_xCoO_2 (0.5>x>1) is oxidized and LCO releases a lithium ion into the electrolyte. Working from here, the Butler-Volmer formulation provided below (Eq. 12) can be used to derive an important expression for the exchange current (i_o) leading to a relationship between the charge transfer resistance and the heterogeneous kinetic rate constant.

$$i = FAk^o\left[C_O(0,t)\exp\left(-\alpha f(E-E^o)\right) - C_R(0,t)\exp[(1-\alpha)f(E-E^o)]\right] \quad (12)$$

$$i_o = FAk^oC \text{ for } \mathrm{CR} = \mathrm{CO} = \mathrm{C}, \text{and } i = i_o f\eta \text{ when } \eta \text{ is very small} \quad (13)$$

$$R_{CT} = \frac{RT}{Fi_o} \rightarrow \boldsymbol{R_{CT} = \frac{RT}{F^2AC\cdot k^o}} \quad (14)$$

The value $E-E^o$ is the voltage overpotential known by the symbol η, f is used instead of $\frac{F}{RT}$ which each hold their usual meaning, where *i* stands for the instantaneous current and C the oxidized and reduced redox species concentrations. On the basis of this derivation, so long as the charge transfer resistance can be obtained reliably from an equivalent circuit model using a Nyquist plot, the heterogeneous rate constant can be obtained. One of the key drawbacks to relying on an impedance equivalent circuit for HRC data is the occasional inability of EIS to provide unambiguous results for R_{CT}. For $LiCoO_2$ cathodes, and utilized effectively for other cathode

chemistries, an equivalent circuit as shown in Figure 15 is employed with two parallel circuits in series, and incorporating a Warburg diffusive contribution in the second parallel circuit. This equivalent circuit is widely used for battery electrodes to model the "solution resistance" (or "series resistance" if describing a compilation of relatively small resistances), bulk resistivity, charge transfer interfaces, and diffusive properties of an electrode system. Specifically for lithium cobalt oxide the equivalent circuit in Figure 15 has been shown to be effective for accurately modeling its dynamic response during intercalation.[56,57,61] Nyquist and Bode plots, the meanings of their features, and their modeling with equivalent circuits will be covered later in this section.

Primary Interface:	Bare LCO/PC-$LiClO_4$	Sputtered LiPON/LCO	Atomic Layer Dep LiPON/LCO
Christie's DPSC	$1.1 \cdot 10^{-6}$	$1.2 \cdot 10^{-7}$	$4.9 \cdot 10^{-7}$
Nicholson's CV	$4.8 \cdot 10^{-6}$	$5.3 \cdot 10^{-8}$	$5.9 \cdot 10^{-7}$
Bard, Faulkner's EIS	$2.6 \cdot 10^{-6}$	$5.4 \cdot 10^{-8}$	$1.4 \cdot 10^{-7}$

Table 3: Comparative results for impedance, Nicholson Method, and Sharp's DPSC method in assessing the heterogeneous rate constant (cm/s) of the three systems studied here.

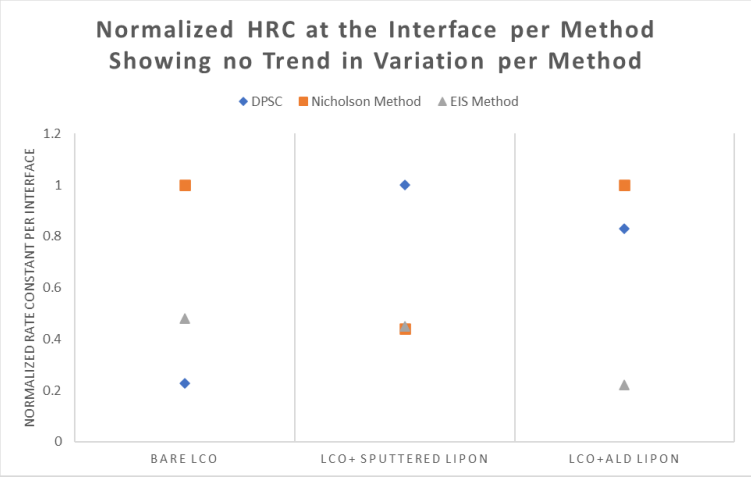

Figure 18: Normalized relationship between distinct EC analysis methods, showing no evidence of under- or over-estimation of the HRC value relative to the alternate computations, nor evidence of trends (e.g. offset-correlation between two or all three methods) in the methods' relationships.

The data presented shows agreement among all three analysis methodologies, with none of the values diverging by more than an order of magnitude. Moreover, it's critical to recognize that due to the inherent nature of these three methods, the comparison is not an ideal 1:1 relationship. For instance, electrochemical impedance measurements can be taken at any point along the reaction coordinate – as represented by the potential in a CV profile (or in the case of galvanostatic processes, the reaction coordinate is represented by time) – as can Christie's DPSC method. On the other hand, the method of Nicholson must be evaluated based solely on the anodic and cathodic peaks of the CV cycle near their specific formal potentials. With regard to this point, Nicholson's method may be accurately thought of as a weighted average of the HRCs at each point along the reaction coordinate - with greater weight being awarded to values closer to the formal potential where the bulk of the electrode's discharge occurs. Furthermore, any analysis involving EIS is, by definition, performed at an equilibrium or quasi-equilibrium state, while Nicholson and Christie's methods measure the rate constant under dynamic conditions. Thus, it is correct to expect some variance between the heterogeneous rate constants of these three methods; the fact that the greatest disparity between methods is 4.4x for liquid electrolyte LCO ("bare LCO"), 2.3x for Sputtered LiPON, and 3.8x for ALD indicates very strong agreement among the methods (Table 3 and Figure 18). It is noted here that very few authors provide a comparative measurement chart of their HRC methodology relative to alternate styles. The use of one methodology over another is of course often dictated by the aim and nature of the study, and the above agreement is a further indicator that well established techniques are largely effective and appropriate.

2.7. Concluding Remarks

Potential step chronoamperometric techniques were applied to the study of ion exchange kinetics at the Li_xCoO_2 interface with either liquid or solid LiPON electrolyte, and to determine the heterogeneous rate constants for each system during anodic and cathodic processes. Impedance scans were taken for the PC-$LiClO_4$/LiPON/Li_xCoO_2 system and provided evidence of strong stability at all contact surfaces. It is found that ion-exchange kinetics for LiPON-Li_xCoO_2 are slower than that of liquid-Li_xCoO_2 in both the anodic and cathodic charge transfer processes. The DPSC technique was capable of divorcing the results of the heterogeneous rate constant from the thickness of the solid electrolyte, suggesting a path forward for fundamental studies of SSE/SE interface kinetics for all scales of battery architecture. Further work by this author will aim to show that the interfacial kinetics where the electrode is poorly conductive are not well correlated to R_{CT} from EIS, and thus that the DPSC methodology provides unique information about electrode reaction kinetics that are not available through alternate methodologies.

3. Determination of the charge-transfer properties at quasi-solid interfaces in ionogel electrolyte systems

3.1. Ionogel Background & Introduction

Room temperature ionic liquids (RTILs) were first discovered over a century ago, but it was not until the 1950s that their potential as a liquid-phase salt was grasped and began to gain traction in the electrochemical field. Defined by a melting point below 100°C, ionic liquids (ILs) such as 1-butyl-3-methylimidazolium bis(trifluoromethylsulfonyl)imide (BMIM TFSI), are essentially molten salts consisting of bulky ions with significant steric hindrance, allowing ILs to remain liquid at very low temperatures. This class of organic compound possesses a wide range

of desirable properties for both safety and performance considerations in contemporary batteries, including wide electrochemical window (1 to 6 V), high thermal stability (beyond 370°C for BMIM-TFSI), negligible vapor pressure, nonflammability, and high conductivity (near 10 mS cm^{-1}).[58-60]

An *ionogel* consists of a porous inorganic gel interpenetrated by an IL, which is held in the network by capillary forces. These structures provide the significant benefit of forming a very thin, solid barrier between opposing electrodes to enhance system safety, while maintaining the properties of liquid wetting at the electrode surface to form optimal interface contact (illustrated diagrammatically in Figure 19). Spun as well as drop-cast ionogels using the methodology of Ashby et al.[43] have conductivities approaching or exceeding those of organic electrolytes, while offering all of the electrochemical and safety enhancements discussed above in regard to the pure ionic liquid electrolytes (ILEs).

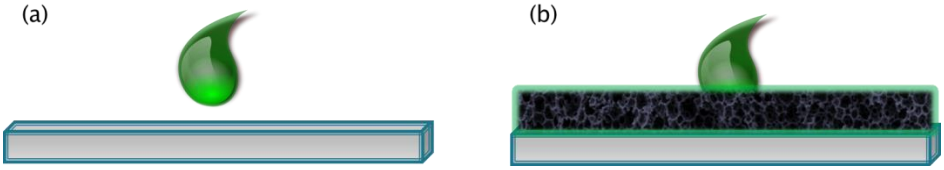

Figure 19: Illustrative representation of the difference between (a) ionic liquid wetting at the platinum electrode, and (b) the ILE impregnated, quasi-solid ionogel drop-cast onto the platinum surface.

The primary drop-cast ionogel structures discussed in this work are fabricated around a sol-gel hydrolysis and condensation route (Figure 20) in which equal volumes of formic acid, TMOS (tetramethoxysilane), and VTEOS (triethoxyvinylsilane) precursors, along with the ionic liquid and cyclohexane, are combined in a 3:3:1 (TMOS/VTEOS/formic acid:ILE:cyclohexane) volumetric ratio.[44] A secondary set of specimen are produced with a lower acid content ratio, favoring the rate of the condensation reaction over hydrolysis and theoretically resulting in

reduced surface area, lower porosity, and relatively smaller pores; these specimen used a ratio of 3:3:0.5 (TMOS/VTEOS/formic acid:ILE:cyclohexane). TMOS and VTEOS are used instead of water for this nonaqueous sol-gel processing rout in order to assert greater control on the rate of condensation, though it should be noted that water is formed and participates as part of the esterification process during condensation.

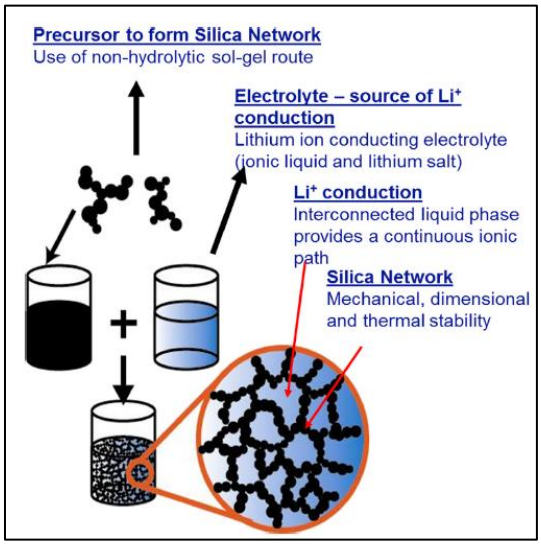

Figure 20: Ionogel general synthesis route (reproduced with permission from author).[43]

As the hydrolysis and condensation reactions proceed, silanol groups (Si-OH) are formed, and later polymerize further into Si-O-Si oxide chains which are suspended in the sol. As the hydrolysis and polycondensation reaction proceeds, viscosity increases until the system becomes a two-phase material consisting of a solid silica network interpenetrated by the ionic liquid. As can be seen in the TEM image in Figure 21, the particular silica network imaged is made up of amorphous particles of 5-10 nm or smaller, having a broad pore size distribution with an average pore diameter of ca. 10 nm.[43] At this stage the ionogel has already been drop-cast onto the electrode of choice while the viscosity is still relatively low, allowing gel solidification to take place over an extended period. It should be noted that while the formic acid present in solution is

known to react and change some electrode surfaces (depending on the surface chemistry), it is well known that noble metals such as platinum are sufficiently resistant to etching via formic acid, and no surface degradation or chemical response is expected.

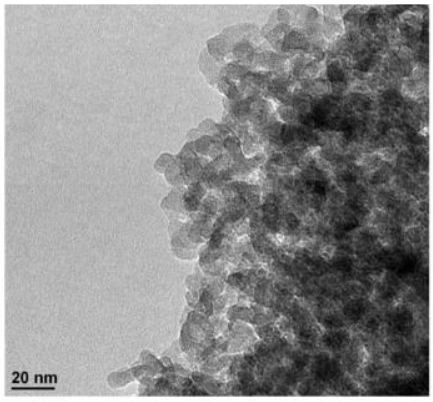

Figure 21: TEM of silica ionogel network with mutual solvent removed.[43]

The nature of the ionogel network and the physical properties of the fabricated sol-gel – including specific surface area, surface-attached ligands and functional groups, pore size distribution, and average pore size – have the ability to alter the observed physiochemical properties of the encapsulated liquid phase within the silicate network, without generating any chemical changes to the liquid itself. These changes generally fall under the umbrella of "confinement effects." Confinement has been studied extensively by researchers such as Dr. Jean Le Bideau of the University of Nantes, France,[75] for both organic and inorganic solid networks in the aim of controlling material properties based on modifying the strength of *ion-wall* interactions relative to *ion-ion* interactions.[67-71]

Furthermore, fully inaccessible pores (those pores or channels that are too small for long-range transport, and which do not allow access of the inner-pore liquid phase into the bulk network) may be in a position to "freeze" electrolyte species into place if they are present during the formation and solidification of the porous silicate network. This may be of interest to

researchers regarding an electrolyte's electronic properties that may be controlled but remain active, even though ionic and molecular transport events are no longer possible.

Recent analogous work on confinement effects of water molecules in capacitive intercalation structures (for example, the well-studied RuO_2 ruthenium dioxide system, and the MnO_2 birnessite structure) has shown that the mass ratio of confined water within layered intercalation materials directly controls the mechanism and availability of interlayer pseudocapacitive ion storage.[78,79] In aqueous electrolytes water molecules act as an ion solvation shell, while when encased within a structured material their electrostatics provide additional spacing between layers. Recent studies provide good evidence that the confinement of water molecules within birnessite control the degree of interaction between the stored ions and the layered oxide slabs, leading to minimized structural changes and charge storage which leads to rectangular CVs and nearly ideal current polarity switching. This mechanism is suggested to occur by increasing the distance between cation and oxide via water mediation, and by providing an ion solvation shell that is roughly ½ as strong as the solvation shell provided to the ion by water molecules in the bulk electrolyte. Such fundamental studies which explore the mechanisms of ion transfer rate clearly provide critical understandings towards developing next-generation storage materials.

3.2. Technique Overview (Reference to Sec. I)

3.2.1. Materials

1-butyl-3-methylimidazolium bis(trifluoromethylsulfonyl)imide (BMIM TFSI, 99.5% purity, etc.) was procured from Solvionic (France), and was degassed on a Schlenk line over 5 hours at 130°C, backfilling with argon gas. After removal from the Schlenk line, the ionic liquid was cooled

and moved into an argon glovebox. Tetramethoxysilane (TMOS, 99% purity), and triethoxyvinylsilane (VTEOS, 98% purity) sol-gel precursors, along with cyclohexane (anhydrous, 99.5% purity) and formic acid (95% purity), were purchased from Sigma Aldrich and used without further purification. Ferrocene powder (99%, packaged under argon) was purchased from Alfa Aesar, and used without further purification. Platinum foil (0.05 mm thickness, 99.99% purity) was purchased from Goodfellow.

3.2.2. Electrode Preparation

The process of depositing drop-cast ionogel specimen has been described previously[43]. Briefly, TMOS and VTEOS are initially combined with formic acid in a 1:1:1 volumetric ratio and mixed for 15 seconds using ultrasonication. Unless otherwise specified, addition of BMIM-TFSI and cyclohexane is carried out in a volumetric ratio of 3:3:1 (TMOS/VTEOS/formic acid):ionic liquid:cyclohexane, while stirring at room temperature. 20 µL of the sol-gel solution is drop cast with micropipette onto the center of an ca. 7 mm by 7 mm surface of rigid, polished platinum foil, retaining space to act as the current collector. The sol gel process is allowed to proceed at room temperature for 12 hours before drying at 140 C in a vacuum oven.

3.2.3. Methods

Three electrode electrochemical testing was performed on a VMP3 potentiostat from Bio-Logic. Electrochemical impedance spectroscopy was performed between 100 mHz and 1 MHz with 10 mV RMS amplitude. All three-electrode, flooded cell testing was performed using a 3-neck round bottom flask in which reticulated vitreous carbon was employed as both counter electrode (CE) and reference electrode (Ref). Unless otherwise specified, the electrolyte employed to obtain electrochemical data is 10 mM ferrocene (Fc) dispersed in BMIM-TFSI. Bare

platinum electrodes were used to obtain a baseline of the ferrocene electrochemical redox in BMIM-TFSI, and in all cases the reverse side of the platinum working electrodes (WEs) (with and without drop cast ionogel) were made inert by covering with chemically resistant Mylar tape. Testing was carried out assuming planar electrode surfaces, and configured with approximately 3 mm separating the working electrode from both CE and Ref to reduce the contribution of electrolyte resistance to cyclic voltammetry and impedance measurements. Resistance compensation feedback is employed to eliminate artifacts caused by IR resistance upon measurement of the direct current. All cyclic voltammetry (CV) measurements was performed at room temperature. Sweep rates tested span 0.020 V/s through 10 V/s unless otherwise specified. Hysteresis in the CV data was found to be insignificant, indicating an acceptable degree of nonreversible reaction at the platinum working electrode surface.

Low-temperature nitrogen sorption was measured on an accelerated surface area and porosity analyzer ASAP2020 Plus manufactured by Micromeritics Instruments Corp. (Norcross, GA). Specific surface area, micro and mesopore volumes, pore size distribution, and vol. % open porosity were calculated as described in the 2015 IUPAC Technical Report.[76] Nitrogen porosimetry isotherms was additionally used to determine the surface fractal dimension, D_{sf}, which should be equal to the mass fractal dimension, utilizing the Frenkel-Halsey-Hill method demonstrated through:

$$\ln n = \mathrm{C} - (3 - D_s) \ln\left(R\,T \ln\frac{P_0}{P}\right)$$

where n is the quantity of N_2 gas adsorbed in cm^3 STP $g - 1$, P is the measured pressure,and P_0 is the saturation vapor pressure.[77]

The method of Nicholson (previously discussed in Part 1) is used to obtain the heterogeneous rate constant for the study of ferrocene in ionic liquid and in the liquid component of the ionogel. This approach is taken largely because the ferrocene redox behavior and profile in cyclic voltammetry is very predictable, is expected to be and is found to be very well defined in this work – and therefore is highly appropriate for the Nicholson's method analysis using anodic and cathodic CV peak separation.

Nicholson's method[62] involves a log-based graphical relationship, correlating the separation between CV peaks to a translation variable, ψ. The value of ψ is linked to the heterogeneous rate constant by the relationship:

$$\psi = \gamma^{\alpha} k_f^o / \sqrt{\pi a D_{ox}} \tag{15}$$

$$\gamma = (D_{Ox}/D_{Red})^{1/2} \tag{16}$$

$$a = n\mathrm{F}v/\mathrm{RT} \tag{17}$$

The term α is the cathodic transfer coefficient and *v* is the sweep rate (note the Greek term α and the letter *a* are different terms above). Therefore, by pairing with the Randles-Sevcik equation, both the kinetic rate constant along with the simultaneously occurring diffusion rates for oxidized and reduced active species are obtained. The graphical relationship, whose derivation will not be reviewed here, is provided by Nicholson in his seminal paper[64] on the topic and is replicated here (Figure 22).

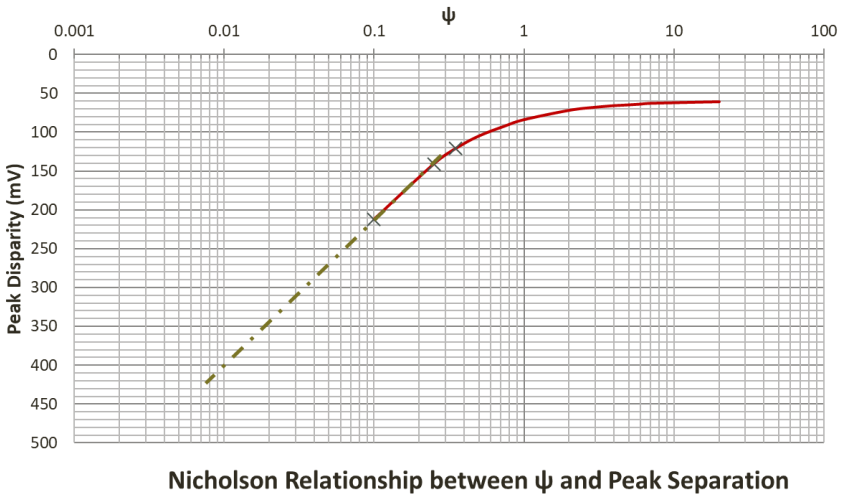

Figure 22: Nicholson's derived graphical relationship to determine the variable ψ from the separation between CV anodic and cathodic peaks.[64]

The Randles-Sevcik equation is used to obtain the values of the diffusion coefficients of ferrocene in BMIM-TFSI ionic liquid and porous ionogels. Though other approaches to obtain D_O and D_R exist, common relationships such as the Stokes-Einstein equation are not appropriate here because Stokes-Einstein theory does not account for charged species states, nor the effects of charged particles or molecules in solution – as is the fundamental characteristic for ionic liquids.[63] The central equation in a Randles-Sevcik analysis is:

$$i_p = 0.4463 \times nFAC_O^* \left(\frac{n\mathrm{F}\nu D_O}{\mathrm{RT}}\right)^{1/2} \quad (18)$$

Known variables have their typical meaning, with *A* representing the electrode geometrical surface area, C^*_O referring to the bulk molar concentration of the oxidized species, and n = 1 for oxidation states of ±1.

3.3. Methodology Standardization to Literature Results

In the aim of establishing that the Nicholson method of determining heterogeneous rate constants is accurate and reliable near the 10^{-3} cm/s rate regime – which is expected of the ferrocene redox couple on platinum in BMIM-TFSI ionic liquid and the respective ionogel – the

tris(2,2-bipyridine)cobalt ($(Co(bpy)_3)^{2+/3+}$ or CoBPY herein) redox couple was used as a standard. Pyati and Murray[65] have detailed the viscosities, diffusion coefficients, and rate constants for a series of electrolyte systems. In this work, we reproduce results from Pyati using polyethylene glycol dimethyl ether of molecular weight 400 (MPEG-400), lithium perchlorate ($LiClO_4$) salt of concentrations 0.020 M and 1.0 M, and 1.0 mM CoBPY in a flooded 3-neck flask. Reticulated vitreous carbon was used as both the reference and counter electrodes, and a cleaned platinum *macro* electrode (ca. 4 x 4 mm exposed in solution) as the working electrode**.** In their work, Pyati and Murray use a CV peak-separation methodology with microdisk electrode, as detailed by Magno et al.[66] to systematically obtain heterogeneous electron transfer rate constants for a wide range of electrolytes of varying concentration using 1.0 mM CoBPY reacting at 25 and 50 μm radius platinum microdisks.

In the work presented here, the mass-basis method was used to calculate the viscosity of the MPEG-400 mixture of MPEG-250 and MPEG-500 (28.5% vol MPEG-250, 71.5 vol% MPEG-500), with 1.0 M and 0.020 M salt concentrations. Further, the measurement of the final 1.0 M and 0.020 M $LiClO_4$ solutions' viscosity was performed directly using the Cannon-Fenske capillary viscometer, and all values compared to those produced by Pyati. Measurements were performed inside of an Argon glovebox and converted to an estimated viscosity in air, using the necessary empirically determined ratio of $\nu_{air}/\nu_{Ar} = 1.20$ at room temperature.

Using MPEG-400 in each case, Pyati and collaborators found the viscosity of 0.020 M $LiClO_4$ to be 14.4 cP; our own findings for the same salt concentration were measured at exactly 14.5 cP. Likewise, for lithium perchlorate concentration of 1.0 M, the Pyati paper finds the viscosity in MPEG-400 to be 45.9 cP, while our results agreed at 46.9 cP. The measurements for

each concentration were taken three times, and the average of the three measurements are reported here in Table 4. Nominal relative pressure in the Argon glove box during measurements was recorded at 1.5 mm Hg. To ensure diffusion coefficients for solute species were equivalent to those found in Pyati, Randles-Sevcik equation is used to obtain the diffusion coefficients for use in Nicholson's cyclic voltammetry-based k^o measurements, while Christie's method for measurement of diffusion coefficients (see citation 32, Christie 1964) is paired with Sharp's double potential step chronoamperometry (DPSC) method of obtaining the heterogeneous rate constant as derived from Christi.e. As reported in Table 4, agreement between Pyati and this work using Randles-Sevcik and Nicholson is very strong, with measured diffusion coefficients having a disparity of ± 11% and the difference for kinetic rate constants at ± 22%, spanning both 0.020 and 1.0 M concentrations.

	$LiClO_4$ Concentration (M)	Viscosity (cP)	Diffusion (cm^2/s)	Kinetic Rate Constant (cm/s)
Pyati (1996)	0.020	14.4	1.6×10^{-7}	$1.2(\pm0.9) \times 10^{-3}$
	1.0	45.9	6.2×10^{-8}	$2.3(\pm0.7) \times 10^{-4}$
Nicholson CV (This Paper)	0.020	14.5	1.8×10^{-7}	$0.94(\pm0.3) \times 10^{-3}$
	1.0	46.9	5.5×10^{-8}	$2.0(\pm0.3) \times 10^{-4}$
DPSC (This Paper)	0.020	16.7	3.6×10^{-6}	$2.0(\pm0.7) \times 10^{-4}$
	1.0	46.9	3.7×10^{-8}	$3.3(\pm0.6) \times 10^{-4}$

Table 4: Comparative results for the assessment of diffusion coefficient and homogeneous kinetic rate constant between Pyati et al., and the work presented here. Use of Randles-Sevcik and the Nicholson method to obtain the diffusion coefficient and the HRC perform well versus the methods and results presented by Pyati et al.

3.4. Primary Results – Reaction Rates of RTIL versus Ionogel Electrolyte

The two distinctive ionogel specimen are denoted by their relative amounts of formic acid catalysts and the corresponding changes in porosity, surface area and pore character. The results

are presented in Table 5 below. The relevant Nitrogen sorption porosity and surface area data were produced by UCLA Graduate Researchers Patricia O'Neil and Danielle Butts.

	Specific Surface Area (m^2/g)	% Porosity	Average Pore Size (nm)	D_{ox} (cm^2/s)	D_{red} (cm^2/s)	k^o(app) (cm/s)	CV Peak Currents (i_a/i_c)
Ionic Liquid	–	–	–	1.5×10^{-7}	1.2×10^{-7}	$3.87(\pm0.3) \times 10^{-3}$	1.0
Ionogel A	676.0	79.2	10.24	5.0×10^{-8}	4.7×10^{-8}	$3.10(\pm0.2) \times 10^{-3}$	1.0
Ionogel B	402.2	66.1	8.81	4.5×10^{-8}	3.6×10^{-8}	$1.71(\pm0.3) \times 10^{-3}$	1.0

Table 5: Comparison of ionic liquid electrolyte versus ionogel electrolyte in surface geometry and kinetic parameters.

The known geometry of the BMIM cation provides that the most theoretically linearized conformation (that is, having no torsion along the nitrogen and carbon backbone) has a length of ca. 10.4 Å.[67] Likewise, the symmetrical conformation of TFSI is found to have diameter of 9.0 Å,[68] while the smallest encapsulated unit within the ionic liquid component electrolyte here – ferrocene – is observed to have diameter of ca. 3.3 Å.[69,70] It must be kept in mind that the *interaction radius* of these charged species, known as the Debye Length, is significantly larger than the atomic diameter or linear size of the molecule itself; and while not simple or trivial to calculate, the Debye Length is equally if not more relevant for wall-molecule interactions within a pore than is its geometrical atomic diameter. Meanwhile, it is recognized that specifically for confinement of the ionic liquid electrolyte BMIM-TFSI, the necessary limit of minimum pore size to observe physical confinement effects (such as kinetics in the current research, but extending to melting temperatures and phase transitions among other physical properties) is approximated at 5 nm and below.[69,71]

Unfortunately, ionogel specimen with pore size below 5 nm were not able to be fabricated with sufficient quality in the attempts from the work presented here. It can be seen in the results

that there is no significant sign of true confinement effects in the kinetics and diffusion properties presented here, though there does appear to be a positive correlation between the magnitude of the diffusion coefficient and average pore size. What is observed in the kinetic data can be postulated to be resultant from a reduced platinum electrode reaction-surface, due to the porosity of the ionogel film at the wetting platinum surface. Additionally, small pore size and a large interaction surface (>400 m^2/g) between network walls and electrolyte are likely to provide some limited restriction to flow, relative to an unrestricted liquid, which has been confirmed elsewhere.[81] It is also well within reason that there is minimal loss of mass transport character as the ionic liquid proceeds through the porous network; that is, the tortuosity based on porosity and pore size distribution for the ionogel specimen tested did not significantly affect the rate of diffusion or charge transfer through the film to the electrode surface.

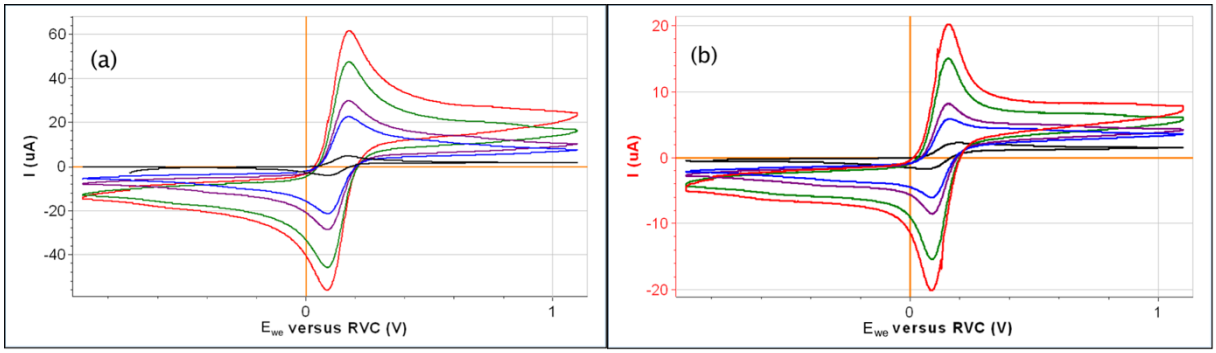

Figure 23: (a) BMIM TFSI Ionic liquid and (b) complimentary ionogel systems, showing cyclic voltammetry compensated for iR_u, at sweep rates of 1, 50, 100, 300 and 500 mV s^{-1}, respectively correlating from smaller to larger current peaks. Peak values from these CVs are used to compute values of the HRC via the method of Nicholson for comparison to Christie et al., as well as the anodic and cathodic peak separation used to compute values of the respective diffusion coefficients via Randles-Sevcik.

It stands to question why the results presented above in comparing IL and ionogel systems are so much more precise (far smaller relative standard deviation) than those obtained with the same method (the method of Nicholson) regarding LCO-LiPON. One reason can be suggested to be the significantly simplified electrochemical system at work with ILs and ionogels. In the IL and

ionogel systems, there are only a single CT interface where a facile redox is taking place (Fc/Fc^{+}), and for which there is no distance between the current collector and the CT surface – unlike the relevant exposed surface of LiPON from part 1, as well as the LCO-electrolyte interface, which are both significantly divorced from the surface of the current collector in the operation of battery materials. Furthermore, there are no concerns with "disorder" near the CT interface, nor with changes in the crystal structure or stoichiometric material properties: There is only a single material in which relevant ion diffusion is occurring, as well as only a single electrolyte; the LCO-LiPON systems discussed have three unique diffusion regions (LCO, LiPON and $LiClO_4$-PC), and two unique electrolytes which act in series with each other.

3.5. Secondary Results – Determining Sharp's DPSC Rate Limitations

The initial methodology used to investigate the heterogeneous rate constant for the ionogel and pure ionic liquid electrolytes in this work is identical to the method first presented by Sharp and Christie et al., and discussed at length in Part 1. Unfortunately, through the course of this work, and prior to establishing the efficacy of Nicholson for the referenced rate values relative to Pyati's work, it has been determined that the DPSC methodology used by Sharp is inappropriate for rates in the regime 10^{1} and greater, through 10^{-3}. Based on the results presented below, while DPSC of Sharp is effective for the regimes near and below 10^{-5} as validated in Part 1, it is not accurate in determining the heterogeneous rate constant of ferrocene in acetonitrile (ACN), nor did it agree with more accurate methods in finding the HRC for ionogel and ionic liquid systems reacting at the platinum electrode shown in this work.

The initial approach to validation of Sharp's DPSC method was to obtain the value of the heterogeneous rate constant of ferrocene dispersed in ACN, and compare to the known values

in literature. Empirically, ferrocene is dispersed in the RTIL electrolyte media and allowed to fully mix, removing water from the solution by means of 0.4 nm sieves, and keeping the ferrocene concentration low to reduce IR resistance based on the magnitude of the currents. It should be mentioned that notable differences in the experimental electrochemical context exist here, relative to the material presented in Part 1. Ionic liquid is typically combined with a lithium salt when used in battery architectures and does not directly perform any redox chemistry during cycling, nor do any of the constituents here perform any kind of intercalation. As such, the ionic liquid electrolytes and ionogels discussed herein are combined with 10 mM dispersed ferrocene, unless otherwise stated, and the reduction and oxidation electrochemistry is measured at a platinum electrode interface in a 3-neck cell architecture housed in an argon glovebox.

Ferrocene is one of the most well studied metallocene molecules used in electrochemical applications. The electron transfer (ET) of the ferrocene/ferrocenium (Fc/Fc^+) redox couple occurs around the formal potential of 0.527 ± 0.018 V vs Ag/Ag^+ with a high rate constant on the order of 1.0 cm s^{-1} when measured in acetonitrile tetrabutylammonium-based electrolytes. In this work, the reference electrode is reticulated vitreous carbon (RVC) for both ILE and ionogel measurements, which has a reference voltage of 0.270 V versus the Ag/Ag^+ standard in acetonitrile. Using the Fc/Fc^+ couple as a standard for electron transfer kinetics, the *relative efficiency* of interface kinetics for the ionic liquid electrolyte and ionogel systems can be probed.

Platinum working electrodes and vitreous carbon counter electrodes were used in the work of Sharp, where acetonitrile (ACN) with $LiClO_4$ supporting salt were used as the electrolyte system.[33] The reference for all measurements in [33] was sodium chloride-calomel electrode

(NaCE) fitted in a glass Luggin capillary with a matching bridge solution for the sample being measured.

For our own work replicating the results of Fc/Fc^+ in $ACN/LiClO_4$, but instead using RVC as the reference electrode and the counter electrode, we were able to obtain values of $k_f^o(app)$ = 0.010 cm s^{-1}, and a transfer coefficient of 0.67, using an electrode having geometrical area of 0.10 cm^2. Cyclic voltammetry of the Fc/Fc^+ redox couple in $ACN/LiClO_4$ is displayed in Figure 24, showing peak separation of 82 mV. The redox response to DPSC at the formal potential is displayed in Figures 25(a) and (b), showing current (I) versus time, and charge (Q) versus square root of time ($t^{1/2}$), respectively. Calculation of the reported values for the cathodic transfer coefficient was performed by determining the slope of $Ln(i_a)$ versus the size of the DPSC step potential ($E-E^o$), following Eq. 11 from Part 1, and is displayed in Figure 26.

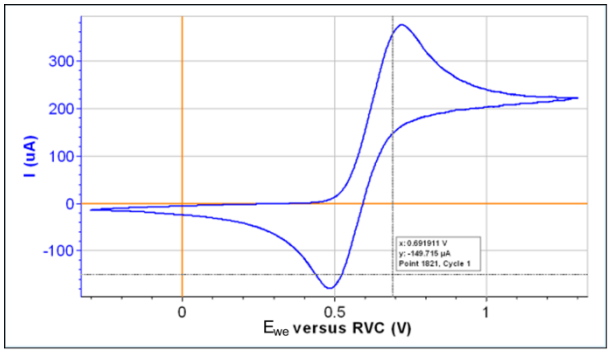

Figure 24: Cyclic voltammetry for Fc/Fc^+ in $ACN/LiClO_4$ on platinum versus RVC counter and reference electrodes, scanning from -0.300 V to 1.300 V, and showing peak separation of 82 mV.

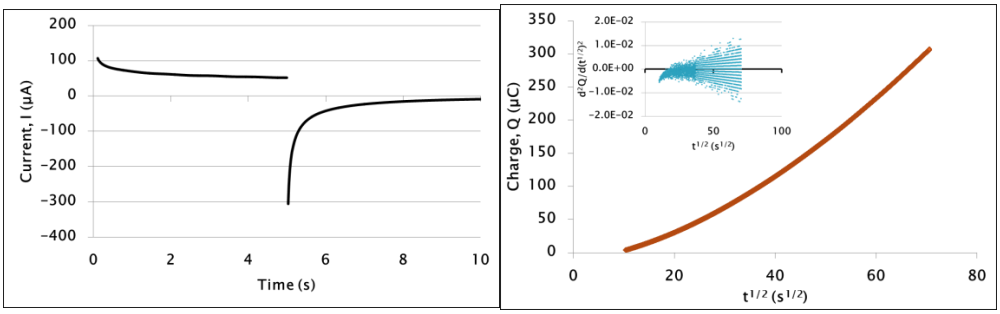

Figure 25: (a) Current transients for anodic double potential step to the formal potential, from $E-E^o$ = -160 mV to $E-E^o$ = 0.0 mV versus RVC and back, with ferrocene dispersed in $ACN/LiClO_4$. (b) Initial anodic formal potential step producing Q vs $t^{1/2}$ approaching linearization around 40 $s^{1/2}$.

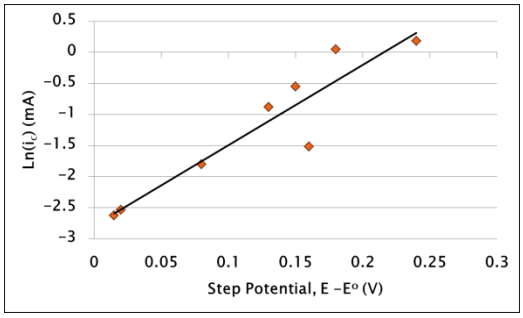

Figure 26: Ln(i_a) versus DPSC voltage-step size for the calculation of the transfer coefficient, α, for ferrocene dispersed in ACN/$LiClO_4$ on platinum foil electrode.

3.6. Results from Sharp's Rate-Limited Methodology

Results from this work using Sharp's DPSC methodology painted a picture describing the impact on the surface kinetic response when converting from a pure ionic liquid electrolyte to the quasi-solid ionogel system. The electrochemical response to DPSC at the formal potentials for the ionic liquid and ionogel electrolyte systems are presented in Figure 27. Figures 27(a) and (c) depict the current response to application of the double potential step, while Figures 27(b) and (d) indicate the degrees of linearization which occur for ILE and ionogel systems, respectively. Working from these data, the obtained apparent formal heterogeneous rate constant, k_f^o(app), for the Fc/Fc^+ couple immersed in pure ionic liquid is measured at 1.7 (±0.4) $x10^{-3}$ cm s^{-1}. This is a significantly higher rate than that measured for the Ferrocene redox occurring in the quasi-solid ionogel, which is found to be 4.2 ((±2.2) $x10^{-5}$ cm s^{-1}. It should be noted that the inset of Figure 27(d) suggests that complete linearization (i.e. $d^2Q/d(t^{1/2})^2$ equal to or rapidly approaching zero for the ionogel electrolyte system is not evident .

It is possible that the time period over which bulk semi-infinite diffusion conditions are valid is shorter than the time scale required to reach linearization with the specific cell geometry used for these samples. Towards this end, Figure 23 demonstrates that cyclic voltammetry at varying scan rates for the Fc/Fc^+ couple in both ILE and ionogel systems is extremely stable,

making for very good conditions to probe the kinetic constants using voltammetric methods, such as Randles-Sevcik and Nicholson as performed above.

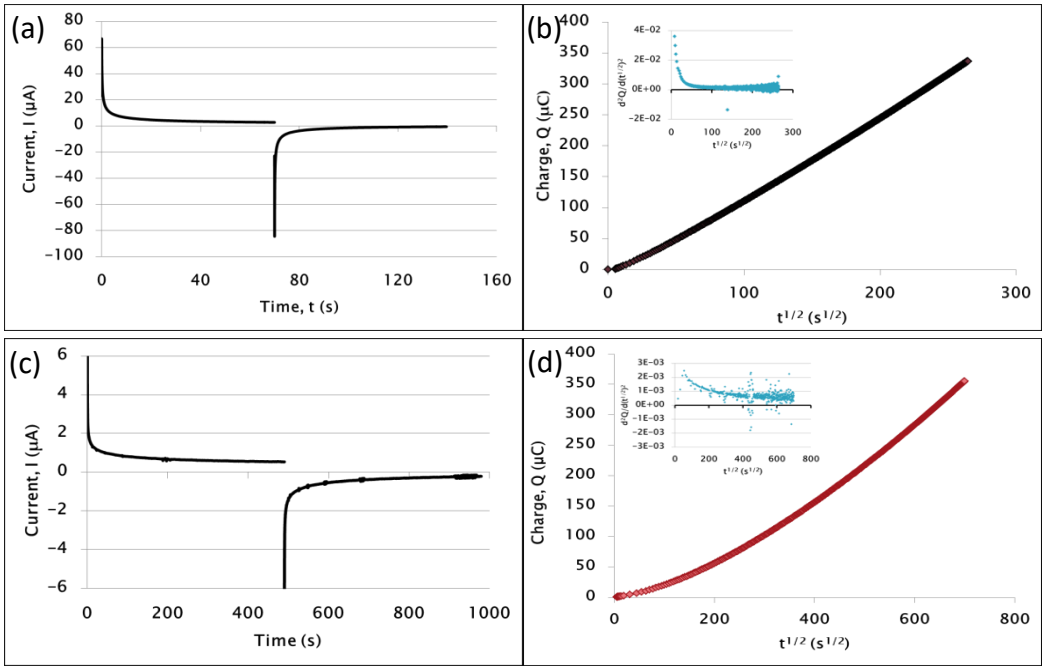

Figure 27: (a) Current transients for anodic double potential step from 0.00V to 340mV versus reticulated vitreous carbon and back, with ferrocene dispersed in BMIM-TFSI ILE on platinum foil electrode. (b) Initial anodic potential step producing Q vs $t^{1/2}$ with linearization clearly evident where the 2nd derivative (inset) centers around zero. (c) (d) (a) Current transients for anodic double potential step from 0.00V to 340mV versus reticulated vitreous carbon and back, with ferrocene dispersed in BMIM-TFSI ILE on platinum foil electrode. (b) Initial anodic potential step producing Q vs $t^{1/2}$, showing the 2nd derivative (inset) where the system approaches linearization but does not reach fully, before semi-infinite bulk diffusion no longer holds.

3.7. Concluding Remarks

A previously studied room-temperature sol-gel process was used to fabricate ionogels of varying average pore diameters in order to study changes in interface and mass transport characteristics based on confinement effects. The method of Nicholson was validated for analysis of the formal rate constants in the range of 10^{-3} cm/s by comparison to results produced by Pyati and Murray[65]. Likewise, Sharp, and Christie's DPSC methodology was found to be inappropriate for kinetic analyses at such high rates – though the same analytical methods were validated by comparison to well-studied kinetic analysis methodologies in part 1, and found to be appropriate

for formal rate constants in the range of those identified for lithium intercalation materials such as $LiCoO_2$, carbon graphite, and $LiMn_2O_4$.

Minimal confinement effects were noted for ionogel pore diameters of 11 nm and 8 nm. However, some loss of mass transport and kinetic rate constants were identified and attributed to both the reduced platinum interaction surface of charge transfer, as well as expected pore wall to electrolyte interaction, which do not exist for free liquid transport. The potential consequences of reactive species and electrolyte confinement have been elucidated with references to recently published works in adjacent charge-storage materials.

4. Suggestions for Future Study

With consideration towards the extensive work performed with thin-film LCO and LiPON materials in part 1 of this thesis, there is some concern that parasitic currents may occur in the background of any thin-film electrochemical systems in which the solid electrolyte does not conformally coat the edges of the film in addition to the surface. The prospective theory is that liquid electrolyte can access, in this case, the Li_xCoO_2 cathode material along the exposed 450 nm edges where there is no LiPON coating; or additionally produce a response at the current collector if the underlying platinum or titanium are unexpectedly reactive to PC-$LiClO_4$. In order to verify that no parasitic currents are taking part in the electron transfer dynamics, samples of $LiCoO_2$-LiPON may be coated at the edges with an epoxy or thin tape that is resistant to the electrolyte and inert to the electrochemical process. Re-measuring cyclic voltammetry profiles as well as comparing results from DPSC analyses will provide evidence of whether parasitic currents are a concern for measurement of electron transfer in thin film electrodes.

Final work from this research can show that the interface kinetics at both liquid and solid-solid interfaces for LCO do not scale relative to the loss of conductivity shown by R_{CT} through EIS, in the Mott insulating voltage region of LCO intercalation. These results are not shown in the present work presented here, and may be published at a later time.

The correlation of interface kinetics to specific surface considerations (deposition processes, solid-solid interactions relative to liquid-solid interactions, etc.) could not be fully confirmed without eliminating any potential correlation of rate constant values respective to the thickness of the solid electrolytes deposited. It is important that future work be performed with access to at least three dissimilar thicknesses of solid electrolyte in contact with identical cathode chemistries, and from identical deposition methods.

The work performed in ionogel kinetics can be continued by probing ionogel synthesis routs to obtain a sufficiently low average pore diameter, in order to identify the inflection point of confinement effects.[69-71,75,81] In light of the impact of inactive species within porous and layered materials within capacitive and pseudocapacitive electrodes,[78,79] it may be of further interest to obtain inactive intercalated species within the layers and channels of intercalation storage materials. While water causes degradation effects in many common battery electrodes, the process to insert non-reactive species within van der Waals layers is well understood – and is commonly performed in 2D nanosheet exfoliation processes.[82,83]

References

1. Luntz, A. C., Voss, J., Reuter, K., Interfacial challenges in solid-state Li ion batteries. *J. Phys. Chem. Lett.* **6**, 4599–4604 (2015).

2. Wang, Y. et al. Design principles for solid-state lithium superionic conductors. *Nat. Mater.* **14,** 1026 (2015).

3. Buschmann, H. et al. Structure and dynamics of the fast lithium ion conductor "Li 7 La 3 Zr 2 O 12." *Phys. Chem. Chem. Phys.* **13,** 19378–19392 (2011).

4. Murugan, R., Thangadurai, V., Weppner, W., Fast lithium ion conduction in garnet-type Li7La3Zr2O12. *Angew. Chemie Int. Ed.* **46,** 7778–7781 (2007).

5. Kato, Y. et al., High-power all-solid-state batteries using sulfide superionic conductors. *Nat. Energy* **1,** 16030 (2016).

6. Wu, B. et al., Interfacial behaviors between lithium ion conductors and electrode materials in various battery systems. *J. Mater. Chem. A* **4,** 15266–15280 (2016).

7. Yamada, I. et al., Lithium-ion transfer at the interfaces between LiCoO2 and LiMn2O4 thin film electrodes and organic electrolytes. *J. Power Sources* **294**, 460-464 (2015).

8. Park, M., Zhang, X., Chung, M., Less, G. B., Sastry, A. M., A review of conduction phenomena in Li-ion batteries. *J. Power Sources* **195(24)**, 7904-7929 (2010).

9. Reimers, J., Dahn, J., Electrochemical and In Situ X-Ray Diffraction Studies of Lithium Intercalation in LixCoO2. *J. Electrochem. Soc.* **139(8)**, 2091 (1992).

10. Levi, M. D. Solid-State Electrochemical Kinetics of Li-Ion Intercalation into Li[1−x]CoO[2]: Simultaneous Application of Electroanalytical Techniques SSCV, PITT, and EIS. *J. Electrochem. Soc.* **146(6)**, 1279 (1999).

11. Fergus, J. W., Recent developments in cathode materials for lithium ion batteries. *J. Power Sources* **195(4),** 939–954 (2010).

12. Whittingham, M. S., Lithium batteries and cathode materials. *Chem. Rev.* **104(10),** 4271–4302 (2004).

13. Ozawa, K., Lithium-ion rechargeable batteries with LiCoO2 and carbon electrodes: the LiCoO2/C system. *Solid State Ionics* **69,** 212–221 (1994).

14. Reisch, M. S., Solid-state batteries inch their way toward commercialization. *Chem. Eng. News* **95,** 19–21 (2017).

15. Talin, A. A., Ruzmetov, D., Kolmakov, A., McKelvey, K., Ware, N., El Gabaly, F., Dunn, B., White, H., Fabrication, testing, and simulation of all-solid-state three-dimensional Li-ion batteries. *ACS Appl. Mater. Interfaces* **8(47),** 32385–32391 (2016).

16. Richards, W. D., Miara, L. J., Wang, Y., Kim, J. C., Ceder, G., Interface Stability in Solid-State Batteries. *Chemistry of Materials* **28(1)**, 266-273 (2016).

17. Dudney, N. J., Addition of a thin-film inorganic solid electrolyte (LiPON) as a protective film in lithium batteries with a liquid electrolyte. *J. Power Sources* **89,** 176–179 (2000).

18. Bates, J. B. et al., Preferred orientation of polycrystalline LiCoO2 films. *J. Electrochem. Soc.* **147,** 59–70 (2000).

19. Iriyama, Y., Kako, T., Yada, C., Abe, T., Ogumi, Z., Reduction of charge transfer resistance at the lithium phosphorus oxynitride/lithium cobalt oxide interface by thermal treatment. *J. Power Sources***146(1-2)**, 745-748 (2005).

20. Gittleson, F. S., El Gabaly, F., Non-Faradaic Li+ Migration and Chemical Coordination across Solid-State Battery Interfaces. *Nano Lett.* **17,** 6974–6982 (2017).

21. Sakuda, A., Hayashi, A., Tatsumisago, M., Interfacial observation between LiCoO2 electrode and Li 2S-P2S5 solid electrolytes of all-solid-state lithium secondary batteries using transmission electron microscopy. *Chem. Mater.* **22(3)**, 949-956 (2010).

22. Kim, K. H. et al., Characterization of the interface between LiCoO2 and Li 7La3Zr2O12 in an all-solid-state rechargeable lithium battery. *J. Power Sources* **196(2)**, 764-767 (2011).

23. Fingerle, M., Buchheit, R., Sicolo, S., Albe, K., Hausbrand, R., Reaction and Space Charge Layer Formation at the LiCoO2–LiPON Interface: Insights on Defect Formation and Ion Energy Level Alignment by a Combined Surface Science–Simulation Approach, *Chem. Mater.* **29,** 7675–7685 (2017).

24. Takada, K. et al., Interfacial modification for high-power solid-state lithium batteries. *Solid State Ionics* **179(27-32)**, 1333-1337 (2008).

25. Jeong, E., Hong, C., Tak, Y., Nam, S. C., Cho, S., Investigation of interfacial resistance between LiCoO2 cathode and LiPON electrolyte in the thin film battery. *J. Power Sources* **159(1)**, 223-226 (2006).

26. Choi, K. H., Jeon, J. H., Park, H. K., Lee, S. M., Electrochemical performance and thermal stability of LiCoO2 cathodes surface-modified with a sputtered thin film of lithium phosphorus oxynitride. *J. Power Sources* **195(24)**, 8317-8321 (2010).

27. Li, J., Dudney, N. J., Nanda, J., Liang, C., Artificial solid electrolyte interphase to address the electrochemical degradation of silicon electrodes. *ACS Appl. Mater. Interfaces* **6(13)**, 10083-10088 (2014).

28. Kim, Y. et al., High voltage stability of LiCoO2 particles with a nano-scale LiPON coating. *Electrochim. Acta* **56,** 6573–6580 (2011).

29. Wang, Z. et al., In Situ STEM-EELS Observation of Nanoscale Interfacial Phenomena in All-Solid-State Batteries. *Nano Lett.* **16,** 3760–3767 (2016).

30. Marcus, R. A., On the Theory of Electron-Transfer Reactions. VI. Unified Treatment for Homogeneous and Electrode Reactions. *J. Chem. Phys.* **43(2)**, 679-701 (1965).

31. Marcus, R. A. Electron Transfer Reactions in Chemistry: Theory and Experiment (Nobel Lecture). *Angewandte Chemie* (International Edition in English) (1993).

32. Christie, J. H., Laurer, G., Osteryoung, R. A. Measurement of charge passed following application of a potential step-application to the study of electrode reactions and adsorption. *J. Electroanal. Chem.* **7,** 60–72 (1964).

33. Sharp, M., Determination of the charge-transfer kinetics of ferrocene at platinum and vitreous carbon electrodes by potential steps chronocoulometry. *Electrochim. Acta* **28,** 301–308 (1983).

34. Bard, A., Faulkner, L., *Electrochemical Methods. Fundamentals and Applications.* (John Wiley and Sons, 1980).

35. Hutzenlaub, T. et al., Three-dimensional electrochemical Li-ion battery modelling featuring a focused ion-beam/scanning electron microscopy based three-phase reconstruction of a LiCoO2 cathode. *AABC Asia 2014 -*

Advanced Automotive Battery Conference, AABTAM Symposium - Advanced Automotive Battery Technology, Application and Market, AABTAM 2014 (2014).

36. Yamakawa, S., Yamasaki, H., Koyama, T., Asahi, R., Numerical study of Li diffusion in polycrystalline LiCoO2. *J. Power Sources* **233**, 199-205 (2013).

37. Marianetti, C. A., Kotliar, G., Ceder, G., A first-order Mott transition in LixCoO2. *Nat. Mater.* **3,** 627 (2004).

38. Xie, J. et al., Orientation dependence of Li-ion diffusion kinetics in LiCoO2 thin films prepared by RF magnetron sputtering. *Solid State Ionics* **179(9)**, 362-370 (2008).

39. Sato, H., Takahashi, D., Nishina, T., Uchida, I. Electrochemical characterization of thin-film LiCoO2 electrodes in propylene carbonate solutions. *J. Power Sources* **68(2)**, 540-544 (1997).

40. Levi, M. D., Aurbach, D., The mechanism of lithium intercalation in graphite film electrodes in aprotic media. Part 1. High resolution slow scan rate cyclic voltammetric studies and modeling. *J. Electroanal. Chem.* **421(1-2)**, 79-88 (1997).

41. Deiss, E., Häringer, D., Novák, P., Haas, O., Modeling of the charge-discharge dynamics of lithium manganese oxide electrodes for lithium-ion batteries. *Electrochim. Acta* **46(26-27)**, 4185-4196 (2001).

42. Lindstrom, H. et al., Li + Ion Insertion in TiO2 (Anatase). 2 . Voltammetry on Nanoporous Films. *J. Phys. Chem. B* **101(39)**, 7717-7722 (1997).

43. Ashby, D. S., DeBlock, R. H., Lai, C. H., Choi, C. S., Dunn, B., Patternable, Solution-Processed Ionogels for Thin-Film Lithium-Ion Electrolytes. *Joule* **2(1)**, 344-358 (2017).

44. Membreno, D., Smith, L., Dunn, B., Silica sol-gel chemistry: Creating materials and architectures for energy generation and storage. *J. Sol-Gel Science and Technology* **70(2)**, 203-215 (2014).

45. Fontaine, O. et al., Mass transport and heterogeneous electron transfer of a ferrocene derivative in a room-temperature ionic liquid. *J. Electroanal. Chem.* **632(1-2)**, 88-96 (2009).

46. Conway, B. E. Two-dimensional and quasi-two-dimensional isotherms for Li intercalation and upd processes at surfaces. *Electrochim. Acta* **38(9)**, 1249-1258 (1993).

47. Kolev, V. L., Danov, K. D., Kralchevsky, P. A., Broze, G. Mehreteab, A., Comparison of the van der Waals and Frumkin adsorption isotherms for sodium dodecyl sulfate at various salt concentrations. *Langmuir* **18(23)**, 9106-9109 (2002).

48. Vorotyntsev, M. A., Badiali, J. P., Short-range electron-ion interaction effects in charging the electroactive polymer films. *Electrochim. Acta* **39(2)**, 289-306 (1994).

49. Chidsey, C. E. D., Murray, R. W., Redox capacity and direct current electron conductivity in electroactive materials. *J. Phys. Chem.* **90(7)**, 1479-1484 (1986).

50. Mathias, M. F., Haas, O., An alternating current impedance model including migration and redox-site interactions at polymer-modified electrodes. *J. Phys. Chem.* **96(7)**, 3174-3182 (1992).

51. Christie, J., Osteryoung, R., Anson, F., Application of Double Potential Step Chronocoulometry to the Study of Reactant Adsorption Theory. *Electroanal. Chem. and Interfacial Electrochem* **13,** 236-244 (1967).

52. Christie, J., Osteryoung, R., Direct Current Effects in Pulse Polarography at the Dropping Mercury Electrode. Electroanal. *Chem. and Interfacial Electrochem* **49,** 301-311 (1974).

53. Wang, Y. Z., et al., Facile Synthesis of Porous LiMn2O4 Spheres as Cathode Materials for High-Power Lithium Ion Batteries. *J. Power Sources* **226**, 140-148 (2013).

54. Forgie, J. C., Kahkani, S. E.,MacNeil, D. D., Rochefort, D., Electrochemical Characterisation of a Lithium-Ion Battery Electrode Based on Mixtures of Carbonates with a Ferrocene-Functionalized Imidazolium Electroactive Ionic Liquid. *Phys. Chem. Chem. Phys.* **20,** 7713-7721 (2013).

55. Chandrasekaran, R., Magasinski, A., Yushin, G., Fuller, T. M., Analysis of a Lithium Insertion/Deinsertion in a Silicon Electrode Particle at Room Temperature. *J. Electrochem. Soc.* **157,** A1139 (2010).

56. Dokko, K., et al., Kinetic Characterization of Single Particles of LiCoO¬¬2 by AC Impedance and Potential Step Methods. *J. Electrochem Soc.* **148,** A422 (2001).

57. Dokko, K., et al., Kinetic Study of Li-Ion Extraction and Insertion at LiMn2O4 Single Particle Electrodes Using Potential Step and Impedance Methods. *J. Electrochem Soc.* **150,** A425(2003).

58. Lewandowski, A., Swiderska-Mocek, A., Ionic Liquids as Electrolytes for Li-ion Batteries – An Overview of Electrochemical studies. *J. Power Sources* **194,** 601-609 (2009).

59. Pandey, S., Analytical Applications of Room-Temperature Ionic Liquids: A Review of Recent Efforts. *Analytica Chemica Acta* **556,** 38-45 (2006).

60. Buzzeo, M., Evans, R., Compton, R., Non-Haloaluminate Room-Temperature Ionic Liquids in Electrochemistry - A Review. *Phys. Chem. Chem. Phys.* **5,** 1106-1120 (2004).

61. Stesmans, A., et al., Electrical Characterization of Ultrathin RF-Sputtered LiPON Layers for Nanoscale Batteries. *ACS Appl. Mater. Interfaces* **8,** 7060-7069 (2016).

62. Nicholson, R. S., Theory and Application of Cyclic Voltammetry for Measurement of Electrode Reaction Kinetics. *Anal. Chem.* **37** (11), 1351-1355 (1965).

63. Katayama, Y., Nakayama, S., Tachikawa, N., Yoshii, K., Electrochemical Behavior of Tris(2,2'-bipyridine)- Cobalt Complex in Some Ionic Liquids. *J. Electrochem. Soc.* **164,** H5286 (2017).

64. Nicholson, R. S., Shain, I., Theory of Stationary Electrode Polarography – Single Scan and Cyclic Methods Applied to Reversible, Irreversible, and Kinetic Systems. *Anal. Chem.* **36** (4), 706-723 (1964).

65. Pyati, R., Murray, R. W., Solvent Dynamics Effects on Heterogeneous Rate Constants of Cobalt Tris(bipyridine). *J. Am. Chem. Soc.* **118,** 1743-1749 (1996).

66. Lavagnini, I., Mango, F., Pastore, P., Application of Cyclic Voltammograms Under Mixed Spherical-Semi-Infinite Linear Diffusion at Microdisk Electrodes for Measurement of Fast Electrode Kinetics. *J. Electroanal. Chem.* **333,** 1-10 (1992).

67. Cha, S., Kim, D., Anion Exchange in Ionic Liquid Mixtures. *Phys. Chem. Chem. Phys.* **17,** 29786-29792 (2015).

68. Elbourne, A., McDonald, S., Voichovsky, K., Endres, F., Warr, G. G, Atkin, R., Nanostructure of the Ionic Liquid – Graphite Stren Layer. *ACS Nano* **9** (7), 7608-7620 (2015).

69. Liu, C., Feng, H., Molecular Dynamic Study of the Behavior of Confined [BMIM][PF6] Ionic Liquids: Pore Size Dependence. *Russ. J. Phys. Chem.* **92,** 2524–2529 (2018).

70. Sriyab, S., Suramitr, S., Hannongbua, S., Prajongtat, P., Encapsulation of Ferrocene in Carbon Nanotubes using Low-Temperature Solution Processing: Influence of Surface Environment, Diameter, and Length, Monatshefte fur Chemie. *Chemical Monthly* **149,** 1963-1969 (2018).

71. Bideau, J. L., Viau, L., Viouz, A., Ionogels, Ionic Liquid Based Hybrid Materials. *Chem. Soc. Rev.* **40,** 907-925 (2011).

72. Kozen, A. C., Pearse, A. J., Lin, C. F., Noked, M., Rubloff, G. W., Atomic Layer Deposition of the Solid Electrolyte LiPON. *Chem. Mater.* **27** (15), 5324-5331 (2015).

73. Gong, C., et al., Surface/Interface Effects on High-Performance Thin-Film All-Solid-State Li-Ion Batteries, *ACS Appl. Mater. Interfaces* **7** (47), 26007-26011 (2015).

74. Fuller, Elliot J., et al., Li-Ion Synaptic Transistor for Low Power Analog Computing. *J. Adv. Mater.* **29** (4), 1604310 (2017).

75. Le Bideu, J., Viau, L., Vioux, A., Ionogels, Ionic Liquid Based Hybrid Materials. *Chem. Soc. Rev.* **40** (2), 907-925 (2011).

76. Thommes, M., Kaneko, K., Neimark, A. V., Olivier, J. P., Rodriguez-Reinoso, F., Rouquerol, J., Sing, K. S., Physisorption of Gases, with Special Reference to the Evaluation of Surface Area and Pore Size Distribution (IUPAC Technical Report). *Pure Appl. Chem.* **87** (9-10), 1051-1069 (2015).

77. Jaroniec, M., Evaluation of the Fractal Dimension from a Single Adsorption Isotherm. *Langmuir* **11** (6), 2316-2317 (1995).

78. Boyde, S., et al., Effects of Interlayer Confinement and Hydration on Capacitive Charge Storage in Birnessite. *Nat. Mater.*, 1-6 (2021).

79. Patrice, S., Gogotsi, Y., Confined Water Controls Capacitance. *Nat. Mater.* **20** (12), 1597-1598 (2021).

80. Garcia, B., Farycy, J., Pererira-Ramos, J. P., Baffier, N., Electrochemical Properties of Low Temperature Crystallized LiCoO2, *J. Electrochem. Soc.* **144(4)**, 1179 (1997).

81. Guyomard-Lack, A., Said, B., Dupre, N., Galarneau, A., Le Bideau, J., Enhancement of Lithium Transport by Controlling the Mesoporosity of Silica Monoliths Filled by Ionic Liquid, *New Journal of Chemistry* **40(5)**, 4269-4276 (2016).

82. Nicolosi, V., Chhowalla, M., Kanatzidis, M. G., Strano, M. S., Coleman, J. N., Liquid Exfoliation of Layered Materials, *Science* **340(6139)** (2013).

83. Coleman, J. N., *et al.*, Two-Dimensional Nanosheets Produced by Liquid Exfoliation of Layered Materials, *Science* **311(6017)**, 568-571 (2011).